

**Key Points:**

- Adopting the improved vegetation emissivity and gravel hydrothermal schemes can obviously improve the frozen soil simulations
- The vegetation emissivity scheme improves the soil surface long-wave radiation heat transfer process
- The gravel hydrothermal scheme improves the thermal properties within the soil

**Correspondence to:**

A. Huang,  
[anhuang@nju.edu.cn](mailto:anhuang@nju.edu.cn)

**Citation:**

Luo, J., Huang, A., Lyu, S., Lin, Z., Gu, C., Li, Z., et al. (2023). Improved performance of CLM5.0 model in frozen soil simulation over Tibetan Plateau by implementing the vegetation emissivity and gravel hydrothermal schemes. *Journal of Geophysical Research: Atmospheres*, 128, e2022JD038021. <https://doi.org/10.1029/2022JD038021>



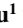
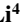
Received 12 OCT 2022  
 Accepted 2 MAR 2023

**Author Contributions:**

**Conceptualization:** Anning Huang  
**Data curation:** Jiangxin Luo, Chunlei Gu, Zhaoguo Li, Wen Zhao, Wanqing Liu  
**Formal analysis:** Jiangxin Luo, Shihua Lyu, Chunlei Gu  
**Funding acquisition:** Anning Huang  
**Investigation:** Jiangxin Luo, Anning Huang, Shihua Lyu, Zhaohui Lin, Chunlei Gu  
**Methodology:** Jiangxin Luo, Anning Huang  
**Resources:** Jiangxin Luo, Zhaohui Lin, Wen Zhao, Wanqing Liu  
**Software:** Jiangxin Luo, Chunlei Gu  
**Supervision:** Anning Huang  
**Validation:** Jiangxin Luo, Anning Huang  
**Visualization:** Jiangxin Luo  
**Writing – original draft:** Jiangxin Luo, Anning Huang, Shihua Lyu  
**Writing – review & editing:** Jiangxin Luo, Anning Huang, Zhaohui Lin, Zhaoguo Li

© 2023. American Geophysical Union.  
 All Rights Reserved.

## Improved Performance of CLM5.0 Model in Frozen Soil Simulation Over Tibetan Plateau by Implementing the Vegetation Emissivity and Gravel Hydrothermal Schemes

Jiangxin Luo<sup>1</sup>, Anning Huang<sup>1</sup> , Shihua Lyu<sup>2</sup> , Zhaohui Lin<sup>3</sup> , Chunlei Gu<sup>1</sup> , Zhaoguo Li<sup>4</sup> , Mingshan Deng<sup>4</sup>, Wen Zhao<sup>5</sup>, and Wanqing Liu<sup>6</sup>

<sup>1</sup>CMA-NJU Joint Laboratory for Climate Prediction Studies, School of Atmospheric Sciences, Frontiers Science Center for Critical Earth Material Cycling, Nanjing University, Nanjing, China, <sup>2</sup>School of Atmospheric Sciences, Chengdu University of Information Technology, Chengdu, China, <sup>3</sup>International Center for Climate and Environment Science, Institute of Atmospheric Physics, Chinese Academy of Sciences, Beijing, China, <sup>4</sup>Key Laboratory of Land Surface Process and Climate Change in Cold and Arid Regions, Northwest Institute of Eco-Environment and Resources, Chinese Academy of Sciences, Lanzhou, China, <sup>5</sup>Linyi Meteorological Bureau, Linyi, China, <sup>6</sup>Wuhai Meteorological Bureau of Inner Mongolia Autonomous Region, Wuhai, China

**Abstract** Frozen soil is widely distributed over the Tibetan Plateau (TP) and has significant impacts on the regional climate and ecosystem. However, the Community Land Model version 5 (CLM5.0) produces evident cold bias in the frozen soil simulation over TP. In this study, an improved vegetation emissivity scheme and a gravel hydrothermal scheme have been implemented into CLM5.0 model, and their synergistic influences on the frozen soil simulation over TP have been systematically addressed and revealed. Results show that adopting the vegetation emissivity scheme, the gravel hydrothermal scheme, and both can remarkably reduce the cold bias in the frozen soil simulated by the original CLM5.0 model, and the column mean root-mean-square error (RMSE) can be reduced by 12.88%, 20.68%, and 31.11% at Arou site and 25.03%, 10.15%, and 36.87% at Maqu site, respectively. The reductions of column mean RMSE for the modeled soil temperature regionally averaged over TP induced by the adoption of vegetation emissivity scheme, the gravel hydrothermal scheme, and both are 32.34%, 6.75%, and 30.18%, respectively. The underlying physical mechanisms are related to the improved representation of the soil hydrothermal processes above or in the soil. The improved vegetation emissivity scheme improves the soil surface long-wave radiation heat transfer process, while the gravel hydrothermal scheme improves the hydrothermal properties within the soil. Overall, improving the surface long-wave radiation heat transfer and the internal soil hydrothermal properties can obviously enhance the performance of CLM5.0 model in simulating the soil freeze–thaw processes.

**Plain Language Summary** The frozen soil over the Tibetan Plateau (TP) exerts evident influences on regional climate and ecosystem. However, the Community Land Model version 5 (CLM5.0) produces obvious cold bias in the frozen soil simulation over the TP due to the inaccurate hydrothermal transfer processes parameterization above or within the soil. Here, we implemented the gravel hydrothermal scheme and the improved vegetation emissivity scheme into CLM5.0 to improve the model performance in simulating the frozen soil over TP. The results from the single-point and regional simulations consistently show that the cold bias in the frozen soil simulation produced by the original CLM5.0 model can be clearly reduced by adopting the improved vegetation emissivity scheme and gravel hydrothermal scheme, indicating that accurate parameterization of hydrothermal transfer processes above or within the soil is equally important to improve the frozen soil simulation and benefits to advance our understanding of the soil freeze–thaw process.

### 1. Introduction

The land surface process plays a critical role in land–air mass and energy exchanges, which greatly affects the weather and climate at local and regional scales (Guo & Wang, 2013; Guo et al., 2011; Lin et al., 1996; Vecellio et al., 2019). The Tibetan Plateau (TP), with an average elevation of 4,000 m, has a wide distribution of seasonally frozen soil and permafrost (Ran et al., 2012; Zou et al., 2017). The soil freeze–thaw process over the TP significantly influences the local climate and even affects the variation of the Asia Summer Monsoon (Gao et al., 2005; C. H. Wang et al., 2020; K. Yang et al., 2013). Therefore, the hydrothermal properties of the soil over the TP in

winter and spring are good indicators for the prediction of the following summer precipitation over eastern China and even the whole of East Asia (Ullah et al., 2021; K. Yang & Wang, 2019a, 2019b).

Frozen soil is a large carbon reservoir with carbon storage nearly twice as much as the atmosphere, and it has positive feedback on the global warming (Schuur et al., 2008; X. J. Wang et al., 2022). Under the global warming, the frozen soil is enduring dramatic degradation. The frozen soil temperature and active layer thickness are increasing (Akerman & Johansson, 2008; Biskaborn et al., 2019; Peng et al., 2018; Vasiliev et al., 2020; Q. B. Wu & Zhang, 2010). The delayed onset of freezing timing and the advanced onset of thawing result in a shorter annual frozen duration (Guo & Wang, 2013; Li et al., 2021; S. Q. Luo et al., 2020). The frozen soil area apparently decreases and gradually retreats to the regions with higher elevations and latitudes (Guo & Wang, 2016, 2017a, 2017b; H. J. Jin et al., 2000). Moreover, the emission of greenhouse gases induced by the frozen soil degradation will undoubtedly exacerbate global warming (Elberling et al., 2013; Schuur et al., 2015).

Land surface models have been widely used to understand the land surface hydrothermal processes and further been coupled with meteorological models for weather and climate prediction (Dai et al., 2003; Lawrence et al., 2019; Niu et al., 2011). To identify the uncertainties of land surface model simulation, considerable efforts have been dedicated recently. S. Q. Luo et al. (2008) modified the frozen soil parameterization scheme in CoLM model to improve the soil liquid water simulation when soil temperature was below the freezing point. C. H. Wang and Yang (2018) incorporated a fully coupled water-heat transport scheme into Community Land Model version 4.5 (CLM4.5) model and improved the simulations of soil temperature and moisture in arid regions. H. L. Liu et al. (2020) optimized the frozen soil parameterization scheme in the Noah-MP model and reproduced the soil freeze–thaw characteristics more realistically. X. D. Zhang et al. (2022) developed a 3D subgrid terrain radiative effect scheme and implemented it into the CoLM model, leading to the soil temperature and moisture simulation biases significantly reduced. Studies on the soil thermal conductivity and hydraulic conductivity parameterizations are more abundant (Fu et al., 2022; H. L. He et al., 2020; S. H. Yang et al., 2021).

Although there are great progresses in the much more realistic representation of the hydrothermal processes among the land surface models, significant uncertainties still exist in the simulations of the soil temperature and moisture, especially for frozen soil (Deng et al., 2020, 2021). This could be attributed to the improper vegetation emissivity scheme which may produce an unrealistic surface radiation budget (X. G. Ma et al., 2019; Mullens, 2013). In addition, in the existing hydrothermal parameterization schemes, the gravel with particle sizes larger than 2 mm is not yet considered in the soil texture data set (Y. G. Liu et al., 2021; Yuan et al., 2021). Actually, it is found that there exists very high content and wide distribution of gravel in the soil over the TP (Arocena et al., 2012; S. Q. Luo et al., 2008; X. D. Wu et al., 2012), and the hydrothermal properties of gravel are completely different from those of fine soils (C. L. Ma et al., 2020; Pan, Lyu, & Gao, 2015).

In this study, we implement an improved vegetation emissivity (VE) scheme and a gravel hydrothermal (GH) scheme into CLM5.0 model and discuss their synergistic effects on the simulation of soil temperature during the soil freeze–thaw period. The findings of this study may provide a better understanding of the soil freeze–thaw process and improve the simulation of frozen soil and thereafter regional climate.

## 2. Study Area

The TP, with a total area of about  $2.5 \times 10^6$  km<sup>2</sup>, is sparsely vegetated but with a very wide distribution of soil gravel content and frozen soil. In winter and spring, the leaf area index (Figure 1a) is less than 0.5 m<sup>2</sup> m<sup>-2</sup> over most part of TP. The soil gravel content at the depth of 0.83 m (Figure 1d) ranges from 30% to 60% with larger values in the west TP. The seasonally frozen soil and permafrost occupy 56% and 40% of the total TP area, respectively (Figure 1e). More than half of the TP area is higher than 4,000 m above sea level (Figure 1f). The topography is complex in the south and north edge of the TP, where the subgrid (3", ~90 m) standard deviation terrain elevation in a grid of  $0.25^\circ \times 0.25^\circ$  can be more than 600 m (Figure 1g).

The locations of two eddy covariance in situ observation sites and two soil temperature and moisture observation networks are shown in Figure 1a. Arou site is a frozen soil superstation and located in a semiarid climate zone over the upper reaches of the Heihe River Basin (Che et al., 2019). The soil texture at Arou site is sandy and gravel (Figure 2a), and the vegetation there is a typical alpine meadow (Su et al., 2020). Maqu site is located in the Yellow River Source Region with a cold and damp climate (Shang et al., 2015; S. Y. Wang et al., 2016). The soil texture at Maqu site is sand–clay–loam (Figure 2b), and the vegetation there is a typical alpine meadow too

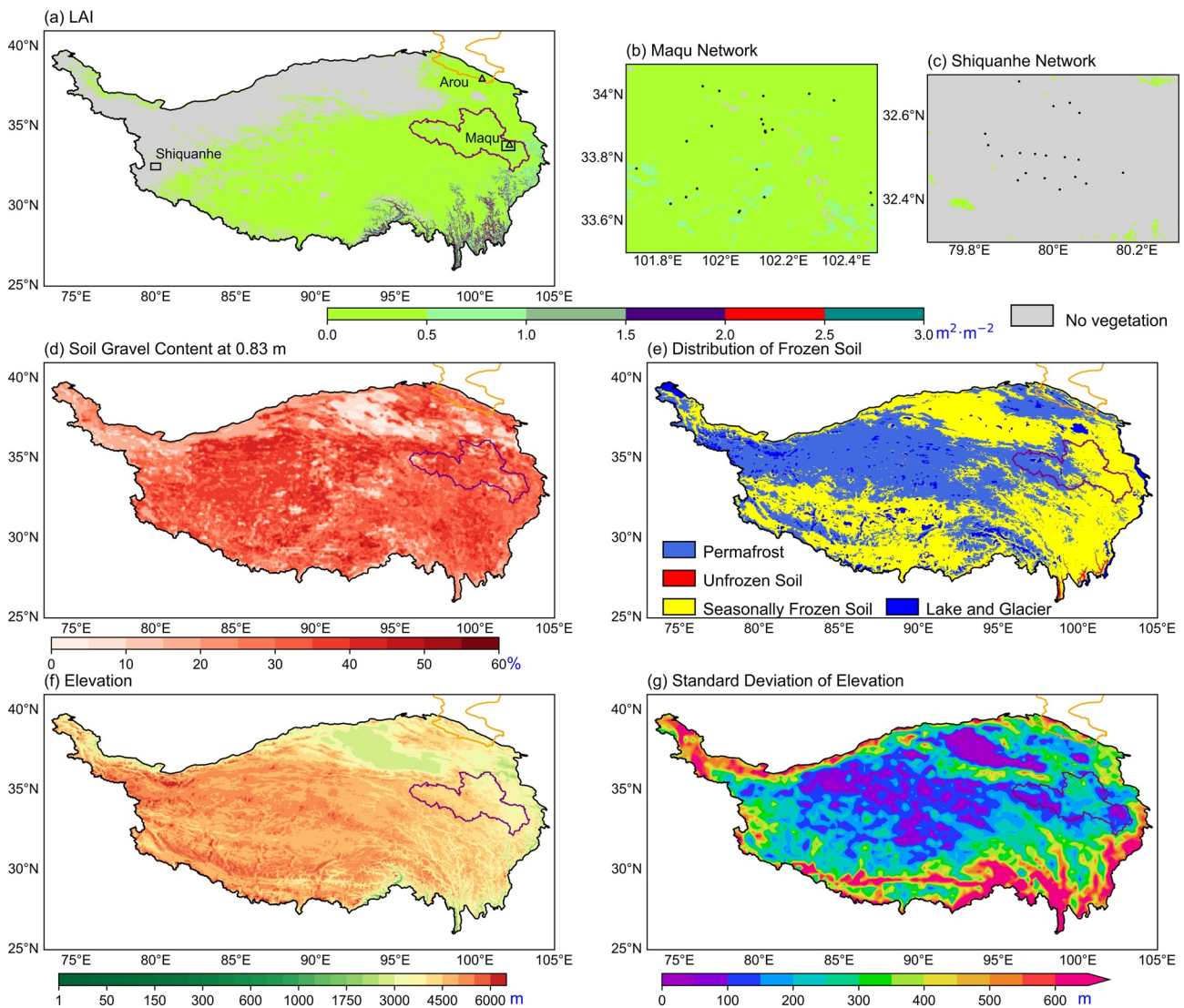


**Figure 1.** The underlying characteristics and the locations of the in situ sites over the Tibetan Plateau. (a) The MODIS leaf area index from October 2013 to May 2014. The sites of Maqu (b) and Shiquanhe (c) observation networks. (d) The soil gravel content at 0.83 m derived from Shangguan et al. (2014). (e) The distribution of frozen soil from Zou et al. (2017). Distributions of the terrain elevation with the horizontal resolution of 3" (f) and the standard deviation of subgrid (3", ~90 m) terrain elevation within the grid of 0.25° horizontal resolution (g). The orange (purple) line indicates the Heihe River Basin (Yellow River Source Region).

(S. Q. Luo et al., 2017). The Maqu network is located at the northeastern edge of the TP with a cold and humid climate. The Shiquanhe network is located in the western part of the TP with a cold arid climate, and the land cover there is dominated by a desert system (P. Zhang et al., 2022). The sites of the two networks are shown in Figures 1b and 1c. These two sites and two soil temperature and moisture observation networks provide representative coverage of vegetation and soil gravel content over the TP.

### 3. Model, Physical Schemes, Data, Experimental Design, and Methods

#### 3.1. Model

The CLM is developed and maintained by the National Center for Atmospheric Research (NCAR). The CLM has been widely used to study the land–air interaction for its sophisticated physical mechanisms (Guo & Wang, 2013; S. Q. Luo et al., 2017, 2018; Xie et al., 2019). Although the latest version of CLM model (CLM5.0) shares the same frozen soil parameterization scheme with the CLM4.5 (Lawrence et al., 2012; C. H. Wang & Yang, 2018), the new features of CLM5.0, such as the dry surface layer for ground evaporation, and the new fresh snow density

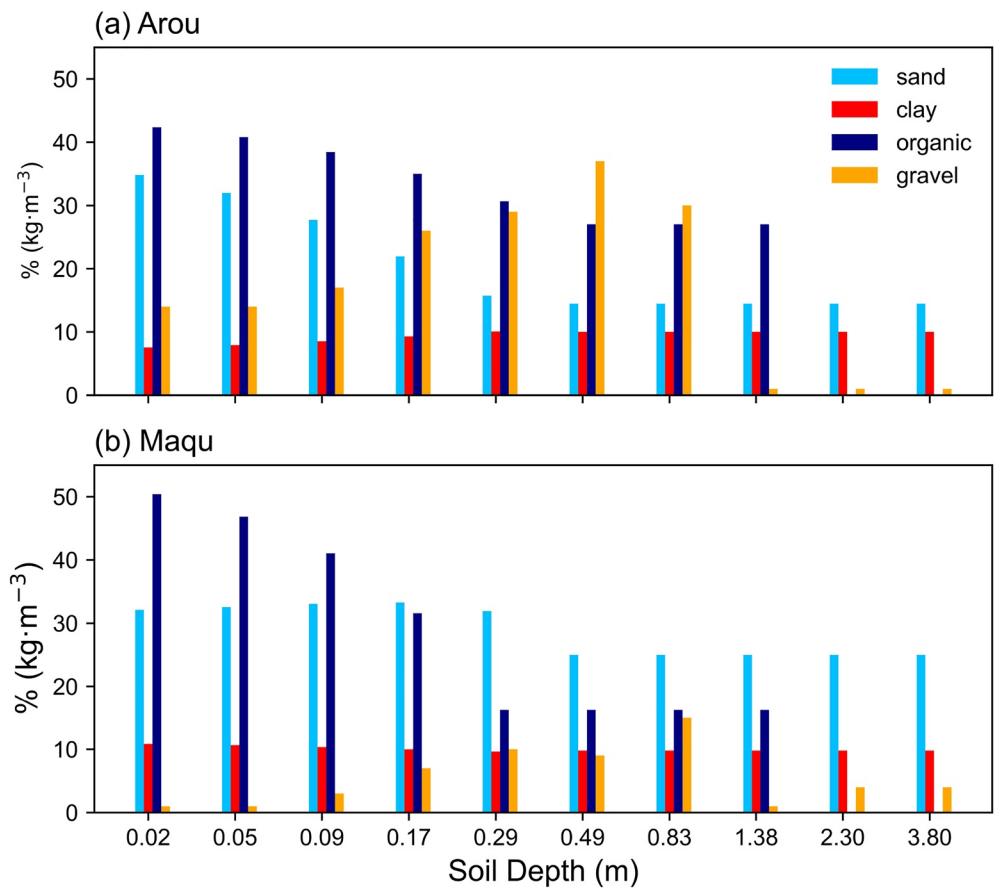


**Figure 2.** Soil texture at Arou and Maqu sites. The unit for sand, clay, and gravel is %, for organic is kg m<sup>-3</sup>.

scheme modified with wind speed and air temperature, offer it a better representation of the soil hydrothermal processes (Deng et al., 2020; Lawrence et al., 2019).

### 3.2. Physical Schemes

X. G. Ma et al. (2019) reported that the VE scheme in CLM4.5 produced unreasonably low VE in the areas with low vegetation density, such as TP (Zhong et al., 2010), and the improved VE scheme (Mullens, 2013) can simulate more accurate snow process in the Northern Hemisphere. Adopting the GH scheme developed by Pan, Lyu, and Gao (2015) and Pan, Lyu, Li, et al. (2015) clearly improved the land surface process simulation over the TP in warm seasons (Y. G. Liu et al., 2021; C. L. Ma et al., 2020; Yuan et al., 2021). We implement the two hydrothermal schemes mentioned above into CLM5.0 model and discuss their synergistic effects on the simulation of soil temperature during the soil freeze–thaw period. Sections 3.2.1 and 3.2.2 introduce the details of the improved VE scheme and the GH scheme, respectively.

#### 3.2.1. Vegetation Emissivity Parameterization

The surface energy balance equation is expressed as

$$G = \overline{S_g} - \overline{L_g} - H_g - \lambda E_g \quad (1)$$

where  $G$ ,  $\overline{S_g}$ ,  $\overline{L_g}$ ,  $H_g$ , and  $\lambda E_g$  are the ground heat flux (positive downward), the solar radiation absorbed by the ground (positive downward), the surface net long-wave radiation emitted from the ground (positive upward), the sensible heat flux (positive upward), and the latent heat flux (positive upward). The unit for each term of Equation 1 is W m<sup>-2</sup>.

The vegetation emissivity ( $\epsilon_v$ ) and ground emissivity ( $\epsilon_g$ ) in CLM5.0 are given by

**Table 1**  
Maximum Leaf and Steam Area Indices and Emissivity of Different PFTs in CLM5.0

PFTs	LAI <sub>pf<sub>t</sub>,max</sub> + SAI <sub>pf<sub>t</sub>,max</sub>	ε <sub>pf<sub>t</sub>,max</sub>
Needleleaf evergreen temperate tree	6.0	0.982
Needleleaf evergreen boreal tree	6.0	0.982
Needleleaf deciduous boreal tree	6.0	0.985
Broadleaf evergreen tropical tree	8.0	0.978
Broadleaf evergreen temperate tree	8.0	0.981
Broadleaf deciduous tropical tree	7.7	0.982
Broadleaf deciduous temperate tree	8.0	0.970
Broadleaf deciduous boreal tree	6.0	0.968
Broadleaf evergreen shrub	5.8	0.987
Broadleaf deciduous temperate shrub	6.3	0.987
Broadleaf deciduous boreal shrub	5.4	0.987
C3 Arctic grass	5.2	0.978
C3 non-Arctic grass	5.9	0.978
C4 grass	5.9	0.978
C3 crop	4.1	0.976
C3 irrigated	4.1	0.981

$$\epsilon_v = 1 - e^{-(\text{ELAI} + \text{ESAI})/\bar{\mu}} \quad (2)$$

$$\epsilon_g = \epsilon_{\text{soil}}(1 - f_{\text{sno}}) + \epsilon_{\text{sno}}f_{\text{sno}} \quad (3)$$

where ELAI, ESAI,  $\bar{\mu}$ ,  $\epsilon_{\text{soil}}$ ,  $\epsilon_{\text{sno}}$ , and  $f_{\text{sno}}$  are the leaf area index, the steam area index, the average inverse optical depth for long-wave radiation, the soil emissivity, the snow emissivity, and the snow cover fraction, respectively.  $\bar{\mu}$  is set to 1.0.

For the vegetated areas, the upward long-wave radiation from the ground is

$$L_g \uparrow = \epsilon_g \sigma T_g^4 + (1 - \epsilon_g) L_v \downarrow \quad (4)$$

where  $\sigma = 5.67 \times 10^{-8} \text{ W m}^{-2} \text{ K}^{-4}$  is the Stefan-Boltzmann constant,  $T_g$  (K) is the ground temperature,  $L_v \downarrow = \epsilon_v \sigma T_v^4 + (1 - \epsilon_v) L_{\text{atm}} \downarrow$  is the downward long-wave radiation ( $\text{W m}^{-2}$ ) below the vegetation,  $T_v$  (K) is the vegetation temperature, and  $L_{\text{atm}} \downarrow$  is the atmospheric downward long-wave radiation ( $\text{W m}^{-2}$ ). Thus, the surface net long-wave radiation is

$$\bar{L}_g = L_g \uparrow - L_v \downarrow = \epsilon_g \sigma T_g^4 - \epsilon_g L_v \downarrow \quad (5)$$

In this study, we replace the original VE scheme in CLM5.0 with the VE scheme improved by Mullens (2013) which is suitable for the regions with different vegetation densities as follows:

$$\epsilon_v = \left( \frac{\text{ELAI} + \text{ESAI}}{\text{LAI}_{\text{pf<sub>t</sub>,max}} + \text{SAI}_{\text{pf<sub>t</sub>,max}}} \right)^{1/k} \times \epsilon_{\text{pf<sub>t</sub>,max}} \quad (6)$$

where LAI<sub>pf<sub>t</sub>,max</sub>, SAI<sub>pf<sub>t</sub>,max</sub>, and ε<sub>pf<sub>t</sub>,max</sub> are the maximum leaf area index, the maximum steam area index, and the maximum emissivity of different plant functional types (PFTs) in CLM5.0, respectively (Table 1).  $k$  is a tunable unitless parameter and is set to 50 (X. G. Ma et al., 2019).

### 3.2.2. Gravel Hydrothermal Parameterization

The soil thermal and hydraulic properties in CLM5.0 are assumed to be a weighted combination of fine soil minerals, which are determined according to sand and clay contents (sand% and clay%), and organic matter (Lawrence & Slater, 2008). The fine soil mineral hydraulic properties include porosity ( $\theta_{\text{sat,min}}$ ,  $\text{mm}^3 \text{ mm}^{-3}$ ), exponent B ( $B_{\text{min}}$ , unitless), saturated hydraulic conductivity ( $k_{\text{sat,min}}$ ,  $\text{mm s}^{-1}$ ), and saturated matric potential ( $\Psi_{\text{sat,min}}$ , mm), which are expressed by the following equations:

$$\theta_{\text{sat,min}} = 0.489 - 0.00126(\% \text{ sand}) \quad (7)$$

$$B_{\text{min}} = 2.91 + 0.159(\% \text{ clay}) \quad (8)$$

$$k_{\text{sat,min}} = 0.0070556 \times 10^{-0.884 + 0.0153(\% \text{ sand})} \quad (9)$$

$$\Psi_{\text{sat,min}} = -10 \times 10^{1.88 - 0.0131(\% \text{ sand})} \quad (10)$$

The porosity for the GH scheme is determined by Poesen and Lavee (1994):

$$\theta_{\text{sat,min}} = (1 - V_g) \theta_{\text{sat,f}} + V_g \theta_{\text{sat,g}} \quad (11)$$

where  $\theta_{\text{sat,f}}$  is the porosity of fine soil (calculated by Equation 7),  $\theta_{\text{sat,g}}$  is the porosity of gravel, and  $V_g$  is the gravel volumetric content.

The scheme for  $B_{\text{min}}$  modified by Pan, Lyu, and Gao (2015) is applied in the GH scheme:

$$B_{\text{min}} = b_g V_g + B_{\text{min,f}} (1 - V_g) \quad (12)$$

where  $b_g$  is set to 6 and  $B_{\text{min,f}}$  is determined by Equation 8.

The revision of  $k_{\text{sat,min}}$  is proposed by Peck and Watson (1979) based on the  $k_{\text{sat,f}}$  (calculated by Equation 8):

$$k_{\text{sat,min}} = k_{\text{sat,f}} \left[ \frac{2(1 - V_g)}{2 + V_g} \right] \quad (13)$$

Considering the water-holding capacity of gravel, Cousin et al. (2003) expressed the  $\Psi_{\text{sat,min}}$  as

$$\Psi_{\text{sat,min}} = \Psi_{\text{sat,f}}^{1-V_g} \Psi_{\text{sat,g}}^{V_g} \quad (14)$$

where  $\Psi_{\text{sat,g}} = -1.3$  mm according to Pan, Lyu, Li, et al. (2015).

The fine soil mineral thermal properties in CLM5.0 include bulk density ( $\rho_d$ , unit:  $\text{kg m}^{-3}$ ), solid heat capacity ( $C_{s,\text{min}}$ ,  $\text{J m}^{-3} \text{K}^{-1}$ ), solid thermal conductivity ( $\lambda_{s,\text{min}}$ ,  $\text{W m}^{-1} \text{K}^{-1}$ ), dry thermal conductivity ( $\lambda_{\text{dry,min}}$ ,  $\text{W m}^{-1} \text{K}^{-1}$ ), and Kersten number ( $K_e$ , unitless), which are expressed by Equations 15–19:

$$\rho_d = 2,700(1 - \theta_{\text{sat}}) \quad (15)$$

$$C_{s,\text{min}} = \left( \frac{2.128(\% \text{ sand}) + 2.385(\% \text{ clay})}{(\% \text{ sand}) + (\% \text{ clay})} \right) \times 10^6 \quad (16)$$

$$\lambda_{s,\text{min}} = \frac{8.8(\% \text{ sand}) + 2.92(\% \text{ clay})}{(\% \text{ sand}) + (\% \text{ clay})} \quad (17)$$

$$\lambda_{\text{dry,min}} = \frac{0.135\rho_d + 64.7}{2,700 - 0.947\rho_d} \quad (18)$$

$$K_e = \begin{cases} \log(S_r) + 1 \geq 0 & , T \geq T_f \\ S_r & , T < T_f \end{cases} \quad (19)$$

where  $\theta_{\text{sat}}$  ( $\text{mm}^3 \text{mm}^{-3}$ ) is the volumetric water content at saturation,  $S_r$  (unitless) is the soil wetness at saturation,  $T$  (K) is the soil temperature, and  $T_f$  (K) is the freezing temperature.

The revision of  $\rho_d$  is derived from Russo (1983):

$$\rho_d = \rho_{d,f}(1 - V_g) + 2,650V_g \quad (20)$$

where  $\rho_{d,f}$  is the fine soil bulk density calculated by Equation 15.

The expression for  $C_{s,\text{min}}$  is modified by Pan, Lyu, Li, et al. (2015):

$$C_{s,\text{min}} = \left( \frac{2.128(\% \text{ sand}) + 2.385(\% \text{ clay}) + 2.5(\% \text{ gravel})}{(\% \text{ sand}) + (\% \text{ clay}) + (\% \text{ gravel})} \right) \times 10^6 \quad (21)$$

The solid thermal conductivity for the GH scheme of Chen et al. (2012) is given by

$$\lambda_{s,\text{min}} = \lambda_q^{q_0} \lambda_{\text{soc}}^{V_{\text{soc}}} \lambda_0^{1-V_{\text{soc}}-q_0} \quad (22)$$

where  $\lambda_q = 7.7 \text{ W m}^{-1} \text{K}^{-1}$ ,  $\lambda_{\text{soc}} = 0.25 \text{ W m}^{-1} \text{K}^{-1}$ , and  $\lambda_0 = 2.0 \text{ W m}^{-1} \text{K}^{-1}$  are the thermal conductivity for quartz, soil organic matter, and other minerals, respectively.  $q_0$  and  $V_{\text{soc}}$  are volumetric content for quartz and organic.

The  $\lambda_{\text{dry,min}}$  and  $K_e$  for the GH scheme is formulated by Côté and Konrad (2005):

$$\lambda_{\text{dry,min}} = \chi \times 10^{-\eta\theta_{\text{sat}}} \quad (23)$$

$$K_e = \frac{kS_r}{1 + (k - 1)S_r} \quad (24)$$

where  $\chi$ ,  $\eta$ , and  $k$  are empirical parameters which are the average values of gravel soil, natural mineral soil, and fiber soil.  $k$  is 4.6 for unfrozen soil and 1.7 for frozen soil, respectively.  $\chi$  is 1.7 and  $\eta$  is 1.8.

Table 2 gives the details of the main modifications in the GH parameterization scheme.

**Table 2**  
Comparison of the Soil Thermal and Hydraulic Scheme for Original and Gravel in CLM5.0

Parameter	Original scheme	Gravel scheme
$\theta_{\text{sat,min}}$	$0.489 - 0.00126(\% \text{ sand})$	$0.489 - 0.00126(\% \text{ sand}) - 0.00489(\% \text{ gravel})$
$B_{\text{min}}$	$2.91 + 0.159(\% \text{ clay})$	$2.91 + 0.159(\% \text{ clay}) \times (1 - \% \text{ gravel}) + 0.06(\% \text{ gravel})$
$k_{\text{sat,min}}$	$0.0070556 \times 10^{-0.884+0.0153(\% \text{ sand})}$	$0.0070556 \times 10^{-0.884+0.0153(\% \text{ sand})} \times \frac{2(1 - \% \text{ gravel})}{2 + \% \text{ gravel}}$
$\Psi_{\text{sat,min}}$	$-10 \times 10^{1.88-0.0131(\% \text{ sand})}$	$-10 \times 10^{1.88-0.0131(\% \text{ sand})} \times (1 - \% \text{ gravel}) + 1.3(\% \text{ gravel})$
$\rho_d$	$2,700(1 - \theta_{\text{sat}})$	$2,700(1 - \theta_{\text{sat}})(1 - \% \text{ gravel}) + 2,650(\% \text{ gravel})$
$C_{s,\text{min}}$	$\left( \frac{2.128(\% \text{ sand}) + 2.385(\% \text{ clay})}{(\% \text{ sand}) + (\% \text{ clay})} \right) \times 10^6$	$\left( \frac{2.128(\% \text{ sand}) + 2.385(\% \text{ clay}) + 2.5(\% \text{ gravel})}{(\% \text{ sand}) + (\% \text{ clay}) + (\% \text{ gravel})} \right) \times 10^6$
$\lambda_{s,\text{min}}$	$\frac{8.8(\% \text{ sand}) + 2.92(\% \text{ clay})}{(\% \text{ sand}) + (\% \text{ clay})}$	$7.7(\% \text{ sand} + \% \text{ gravel}) \times 2.0^{(1 - (\% \text{ sand} + \% \text{ gravel}))}$
$\lambda_{\text{dry,min}}$	$\frac{0.135\rho_d + 64.7}{2.700 - 0.947\rho_d}$	$1.7 \times 10^{-1.8\theta_{\text{sat}}}$
$K_e$	$\log(S_r) + 1$	$\frac{k_{S_r}}{1 + (k - 1)S_r}$

### 3.3. Data

The observed data at Arou and Maqu sites from 1 January 2013 to 31 May 2014 are used to force the single-point offline simulations. The observed contents of sand, clay, and organic matter for the Arou and Maqu sites are from Su et al. (2020), and the contents of gravel are derived from the data provided by Shanguan et al. (2014) with a horizontal resolution of 5 km. The single-point atmospheric forcing data include air temperature, relative humidity, and wind speed 2 m above the surface, surface pressure, downward shortwave, and long-wave radiation, and precipitation with a half-hourly temporal resolution. From Figure 3, the site observed atmospheric forcing data show obvious seasonal variation. The mean values of air temperature, downward shortwave radiation, downward long-wave radiation, relative humidity, surface pressure, and wind speed are 273.20 (273.97) K, 191.15 (210.30) W m<sup>-2</sup>, 248.11 (257.46) W m<sup>-2</sup>, 53.29 (63.12)%, 728.30 (670.48) hPa, and 2.88 (2.73) m s<sup>-1</sup> at Arou (Maqu) site. The rainfall at Arou and Maqu sites mainly occurs in July while snowfall mainly occurs in April. The regional forcing data from 1 January 2009 to 31 May 2014 are developed by the Institute of Tibetan Plateau Research, Chinese Academy of Sciences (ITP, J. He et al., 2020). It has the same variables as the single-point observation but with a three-hourly temporal resolution and a horizontal resolution of 0.1°. The soil texture data provided by Shanguan et al. (2014), including sand, clay, and gravel contents, are used to conduct the regional simulation too.

The validating data in the period from 1 October 2013 to 31 May 2014 include the observed soil temperature at the depths of 4 (or 5), 10, 20, 40, 80, and 160 cm with a half-hourly temporal resolution at Arou and Maqu sites and the observed soil temperature at the depths of 5, 10, 20, and 40 cm with a 15-min temporal resolution at Maqu and Shiquanhe networks. The hourly China Meteorological Administration Land Data Assimilation System (CLDAS) soil temperature in the same period at the depths of 5, 10, and 40 cm with a horizontal resolution of 0.0625° is used to validate the regional simulations. Additionally, the monthly MODIS (Moderate Resolution Imaging Spectroradiometer) emissivity products (MOD11A2; Z. M. Wan, 2014) from Terra with a horizontal resolution of 0.05° during June 2013 to May 2014, which have good agreement with the in situ observations (M. L. Jin & Liang, 2006; K. Wang et al., 2007), are used to validate the VE scheme simulations.

### 3.4. Experimental Design

As shown in Table 3, four offline experiments at single-point and regional scales are conducted to evaluate the synergistic influences of the improved VE and GH schemes on the CLM5.0 model performance to simulate the frozen soil at Arou and Maqu sites and the whole TP, respectively. The soil vertical discretization is 15 layers in the CLM5.0 model, and the soil temperature is calculated at the depths of 1, 4, 9, 16, 26, 40, 58, 80, 106, 136, 170, 208, 250, 299, and 358 cm (Lawrence et al., 2019). The CTL experiment has been carried out with the original CLM5.0 model, and three sensitive experiments have been conducted with the modified CLM5.0 model as follows: the TE experiment with the improved VE scheme, the TG experiment with the GH scheme, and the TEG experiment with both the GH and the improved VE schemes. All the experiments are independently conducted at Arou and Maqu sites and the whole TP. In each single-point experiment, the CLM5.0 model first runs 100 years cyclically driven by the atmospheric forcing data from 1 January 2013 to 31 December 2013, as the spin-up to

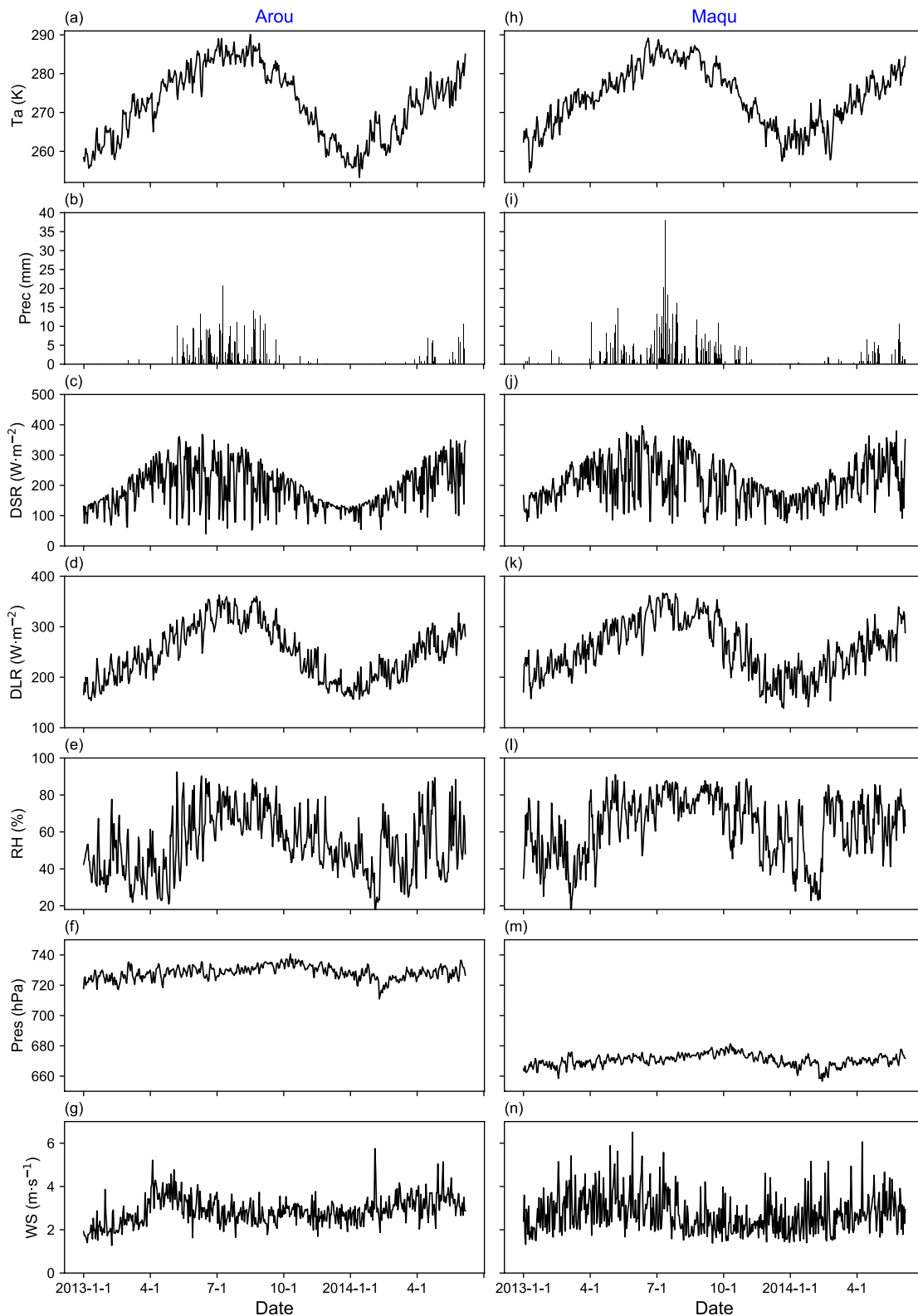


**Figure 3.** The forcing data at Arou and Maqu sites during 1 January 2013 to 31 May 2014. Ta, air temperature; Prec, precipitation; DSR, downward shortwave radiation; DLR, downward long-wave radiation; RH, relative humidity; Pres, surface pressure; WS, wind speed.



**Table 3**  
Design of Experiments by CLM5.0

Cases	Soil texture	VE scheme	GH scheme
CTL	Observation	Off	Off
TE	Observation	On	Off
TG	Observation	Off	On
TEG	Observation	On	On

reach the hydrothermal stability of the soil (Z. L. Yang et al., 1995; Yuan et al., 2021). Then, the CLM5.0 for each single-point experiment runs from 1 January 2013 to 31 May 2014, with the observed atmospheric forcing data and the initial soil temperature and moisture provided by the spin-up run. In each regional experiment, the CLM5.0 model forced by the ITP data runs consecutively from 1 January 2009 to 31 May 2014 at the  $0.25^\circ \times 0.25^\circ$  grids with the first 4 years as the spin-up time (Xie et al., 2019).

### 3.5. Methods

The root-mean-square error (RMSE) and Taylor score (TS; Taylor, 2001) are used to quantitatively evaluate the model performance. The RMSE measures the model errors in quantity and the Taylor score assesses the model performance in reproducing the similarity of the temporal or spatial variability between the simulation and observation. Lower RMSE and higher TS indicate better performance of the model (Huang et al., 2016, 2019). The simulated soil temperature during the freeze–thaw period (from 1 October 2013 to 31 May 2014) is linearly interpolated to the same depth of the observation before doing analysis (S. Q. Luo et al., 2017; J. Y. Wang et al., 2019).

## 4. Results

### 4.1. The Changes in Hydrothermal Parameters Induced by Adopting the VE and GH Schemes

Ogawa et al. (2003) pointed out that the emissivity of vegetation varies from 0.93 to 0.98. As shown in Figure 4, the MODIS retrieved surface emissivity near 0.98 at Arou and Maqu sites displays very small annual variation, but the VE estimated by the CLM5.0 model with the original VE scheme fluctuates sharply with the vegetation dynamics (ranging from 0.42 to 0.90 at Arou site and from 0.54 to 0.95 at Maqu site, respectively). The improved VE scheme produces VE ranging from 0.94 to 0.96 at Arou site and from 0.94 to 0.97 at Maqu site, respectively. Compared to the CTL experiment, the RMSE of the VE at Arou (Maqu) site simulated by the TE experiment with an improved VE scheme against the MODIS observation largely decreases from 0.42 to 0.04 (0.31 to 0.03).

As shown in Figures 5a and 5b, compared to the results from the CTL experiment without considering the effect of gravel, the gravel content directly increases the solid content and reduces the water content in the soil: adopting the GH scheme in CLM5.0 model increases the *B* exponent, bulk density, dry thermal conductivity, and solid heat capacity and decreases the soil porosity, saturated hydraulic conductivity, saturated matric potential, and solid thermal conductivity at both Arou and Maqu sites. Besides, the relative changes in soil hydrothermal properties are related to the amount of gravel content (Figure 2). The large relative changes in soil hydrothermal properties well correspond to high gravel content. Numerically, the GH scheme has the largest impact on the mineral solid

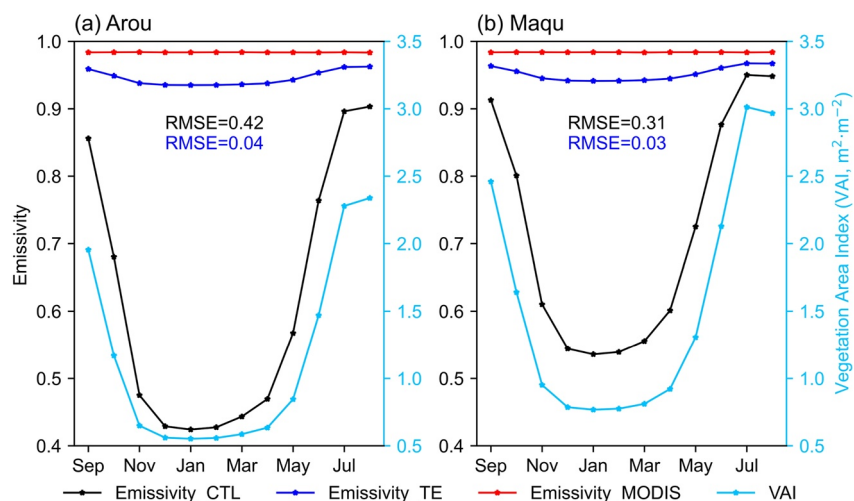


**Figure 4.** The monthly variations of the MODIS derived surface emissivity and the simulated vegetation emissivity from the CTL and TE experiments, and the model input vegetation area index (VAI) at (a) Arou and (b) Maqu sites during June 2013 to May 2014. The MODIS surface emissivity is the value of area average ( $0.1^\circ \times 0.1^\circ$  centered at the in situ site).

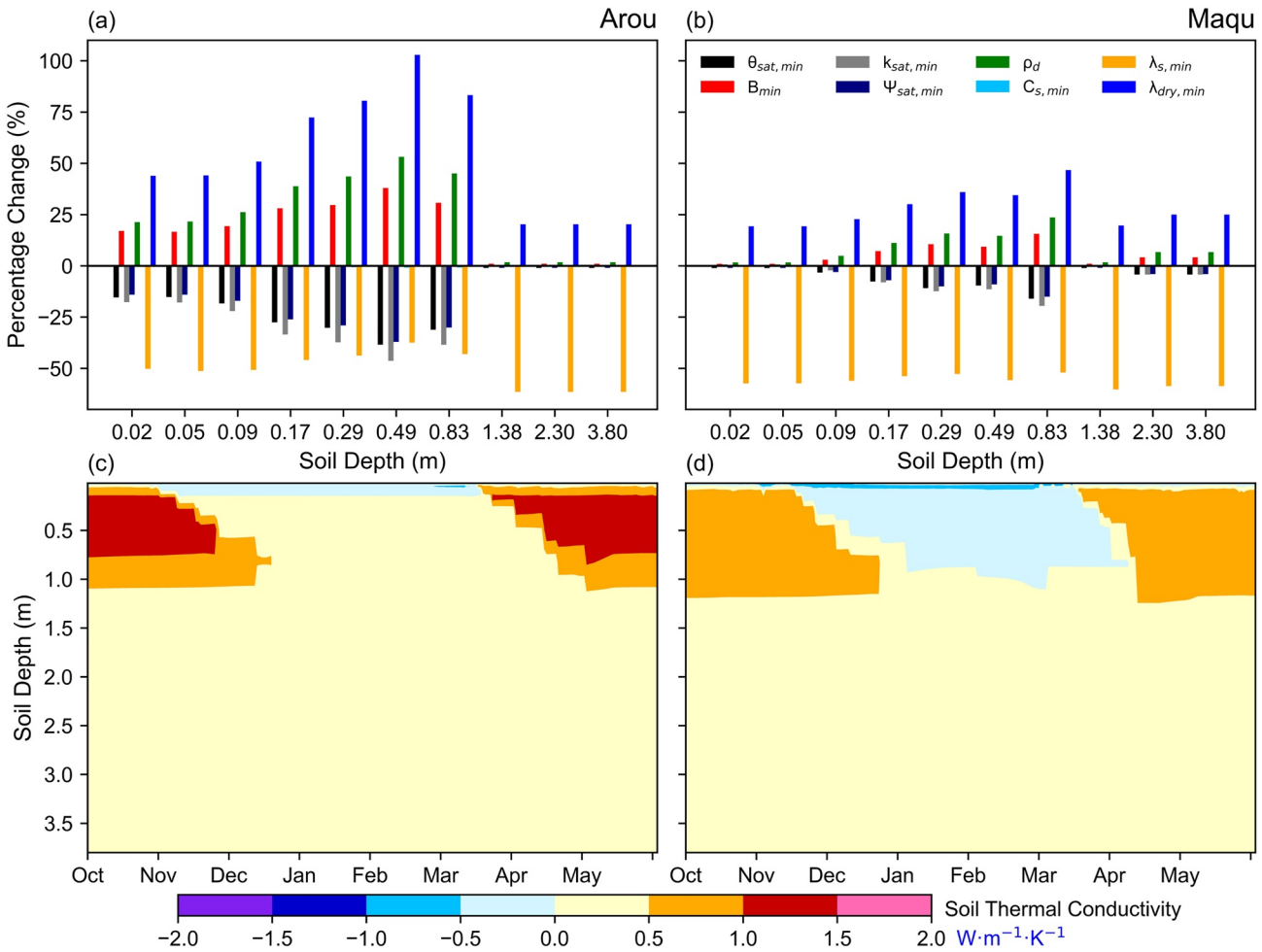


**Figure 5.** The relative changes of soil hydrothermal parameters in the TG experiment compared to the CTL experiment at Arou (a, c) and Maqu (b, d) sites during 1 October 2013 to 31 May 2014.

thermal conductivity and dry thermal conductivity in the soil. The changes in soil mineral hydrothermal properties will further affect the soil heat-water transport process. From Figures 5c and 5d, the GH scheme increases the soil thermal conductivity at the depths of 0.05–3.80 m, especially at the depths of 0.05–1.38 m in October–November and April–May, but it reduces the soil thermal conductivity at upper layers above 0.09 m (0.8 m) at Arou (Maqu) site during December–March when the soil is completely frozen. The effect of GH scheme on heat-water transport process within the soil is complex and depends not only on the amount of gravel content but also on the soil texture, soil liquid water, and ice content (C. L. Ma et al., 2020; Pan, Lyu, & Gao, 2015; Pan, Lyu, Li, et al., 2015).

#### 4.2. The Changes in Soil Surface Heat Fluxes Induced by Adopting the VE and GH Schemes

Figure 6 gives the differences in soil surface heat fluxes between each sensitive experiment (TE, TG, and TEG) and CTL experiment. According to previous studies (S. Q. Luo et al., 2017; J. Y. Wang et al., 2019), the freeze–thaw period can be divided into the freezing period (October–November), the completely frozen period (December–February), and the thawing period (March–May).

During the freeze–thaw period (Figures 6a and 6b), compared to the CTL experiment, the TE experiment generates less surface net long-wave radiation (positive upward) induced by more downward long-wave radiation from the vegetation because of the increased VE and slightly less surface net short wave radiation (positive downward) resulting in more surface net radiation (positive downward) whose intensity is comparable to the magnitude of the surface net long-wave radiation change. Most of the increased surface net radiation is distributed to warm the soil surface (Section 4.5) and thereafter leads to a large increase in the turbulent heat flux (the sum of sensible and

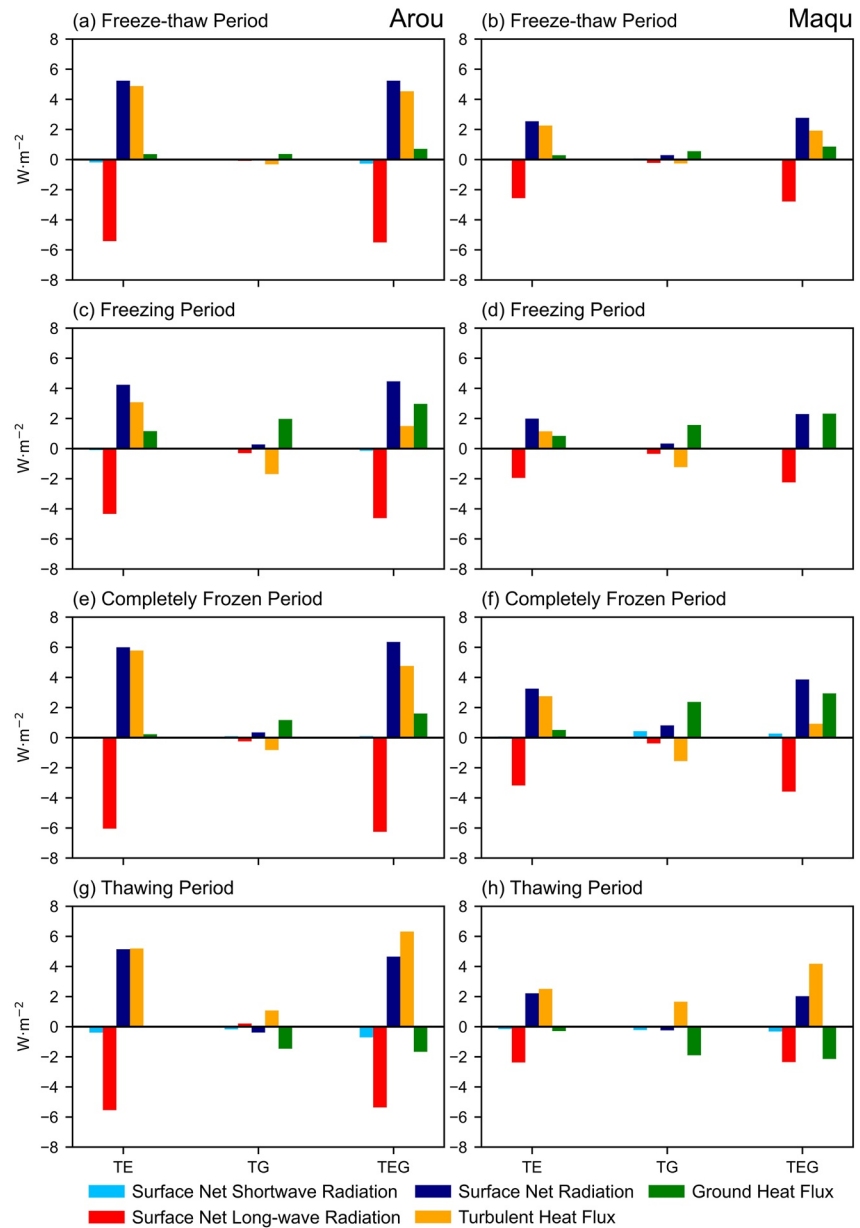


**Figure 6.** The differences in surface heat fluxes between each sensitive experiment and CTL experiment in the freeze–thaw period during 1 October 2013 to 31 May 2014, the freezing period (October–November), the completely frozen period (December–February), and the thawing period (March–May) at Arou and Maqu sites.

latent heat flux, positive upward) and a slight increase in ground heat flux. Due to the much larger increase in VE (Figure 4), the change in each surface heat balance component is relatively larger at Arou site than at Maqu site. Meanwhile, the decrease in the soil thermal conductivity at the soil subsurface layer produced by the TG experiment reduces the heat loss from the soil subsurface to surface representing an increase in ground heat flux and a decrease in ground temperature (Section 4.5). It in turn decreases the turbulent heat flux as well as the surface net long-wave radiation, which further increases the surface net radiation. The changes in each surface heat balance component in the TEG experiment with the VE and GH schemes are the quasilinear superposition of the changes in the TE and TG experiments relative to the CTL experiment.

In the freezing (Figures 6c and 6d) and completely frozen (Figures 6e and 6f) periods, the soil is a heat source and releases the energy from deep soil to the surface (J. X. Luo et al., 2022; J. Y. Wang et al., 2019). The changing features of each surface heat component produced by the TE, TG, and TEG experiments relative to the CTL experiment in the freezing and completely frozen periods are similar to those in the freeze–thaw period.

However, in the thawing period (Figures 6g and 6h), the soil is a heat sink and gains the heat from the surface due to the solar radiation increasing (Figures 3c and 3j). Compared to the CTL experiment, both TE, TG, and TEG experiments produce less ground heat flux into the deep soil layers, indicating that more heat is distributed to heat the surface and less heat into the deeper soil layers, resulting in relatively warmer surface (Section 4.5), which increases the turbulent heat flux and upward surface long-wave radiation. The increase of ground temperature in the TE, TG, and TEG experiments leads to an increase of surface evaporation and thereafter the surface soil liquid water decreased (not shown), which leads to an increase of the surface albedo (not shown) and thereafter a decrease in the surface net shortwave radiation.

### 4.3. The Changes in Single-Point Soil Temperature Simulation Induced by Adopting the VE and GH Schemes

Figure 7 depicts the time–depth distribution of the observed and simulated soil temperature at Arou site. As shown in Figure 7a, the soil temperature fluctuates evidently at the depths ranging from 4 to 40 cm and stabilizes at the depths of 80–160 cm during the freeze–thaw period because the upper layers are more sensitive to the changes in atmospheric forcing conditions. The soil at 4 cm starts to freeze on 3 November and gradually penetrates to deeper layers with a maximum frozen depth larger than 160 cm. Then, the soil starts to thaw on 18 March, and the soil column thaws completely on 21 May, enduring a frozen period of 199 days. It is clear that the CTL experiment (Figures 7b and 7c) can reproduce the overall vertical structure of soil temperature but tends to underestimate it from October to the subsequent March with a bias of  $-1.93^{\circ}\text{C}$  and overestimate it from April to May with a bias of  $1.09^{\circ}\text{C}$ . The soil shows a stronger and more advanced freeze–thaw process in the CTL experiment with a frozen duration of 187 days compared to the observation.

From Figures 7d and 7e, the improved VE and GH schemes can distinctly reduce the cold bias of soil temperature stratification during most time of the freezing and completely frozen periods. The soil freeze–thaw onset and end dates at 4 cm are determined by the atmospheric forcing conditions. As discussed in Section 4.2, the improved VE scheme decreases the upward surface net long-wave radiation, but most of the energy is distributed to warm the soil surface and a small portion is distributed to suppress the heat loss from the deep soil in the freezing and completely frozen periods. Then, the soil temperature produced by the TE experiment in the freezing and completely frozen periods is increased by  $0.64^{\circ}\text{C}$  compared to the CTL experiment (Figure 7d). Furthermore, it delays the freezing process and accelerates the thawing process relative to the CTL experiment, leading to a shorter frozen duration of 172 days and a lower soil ice content, and making it possible to reduce the energy required for soil ablation. The soil temperature produced by the TE experiment in the thawing period is increased by  $0.67^{\circ}\text{C}$  (Figure 7d) even though there is a slight decrease in the ground heat flux compared to the CTL experiment (Figure 6g).

From Figure 7e, compared to the CTL experiment, the decrease of the soil thermal conductivity at the soil subsurface in the TG experiment inhibits the heat loss from the soil subsurface to surface in the freezing and completely frozen periods, which increases soil temperature in November–March. The increase in soil temperature is more obvious at the depths of 20–160 cm because of the higher gravel content. In January, when the cold bias is relatively larger in the CTL experiment, the soil temperature increases much more evidently. In the thawing period, the decrease in the downward ground heat flux decreases soil temperature because it is the main changing feature of soil surface heat fluxes in the TG experiment relative to the CTL experiment.

It is noted that the soil temperature produced by the TEG experiment with both VE and GH schemes adopted is further increased relative to the CTL experiment (Figure 7f). As discussed in Sections 4.1 and 4.2, the VE scheme improves the soil surface long-wave radiation heat transfer process, while the GH scheme improves the hydrothermal properties within the soil, and they have a synergistic effect on the modeled soil temperature. The changes in soil temperature in the TEG experiment adopting the VE and GH schemes are the quasilinear superposition of the changes in the TE and TG experiments relative to the CTL experiment. The difference features in the TE and TG experiments get much more obvious in the TEG experiment during most time of the completely frozen period. Additionally, the freezing front produced by the TEG experiment shows the best agreement with the observation among the four experiments.

The air temperature is higher at Maqu site than at Arou site (Figures 3a and 3b), resulting in higher soil temperature and a weaker freeze–thaw process. From the observation (Figure 8a), the soil surface at Maqu site starts to freeze on 17 November, starts to thaw on 13 March, and thaws completely on 13 April, with a maximum frozen depth of 123 cm and a frozen duration of 116 days. The CTL experiment (Figures 8b and 8c) can reproduce the time–depth distribution of soil temperature but still show an underestimation in October–February with a bias of

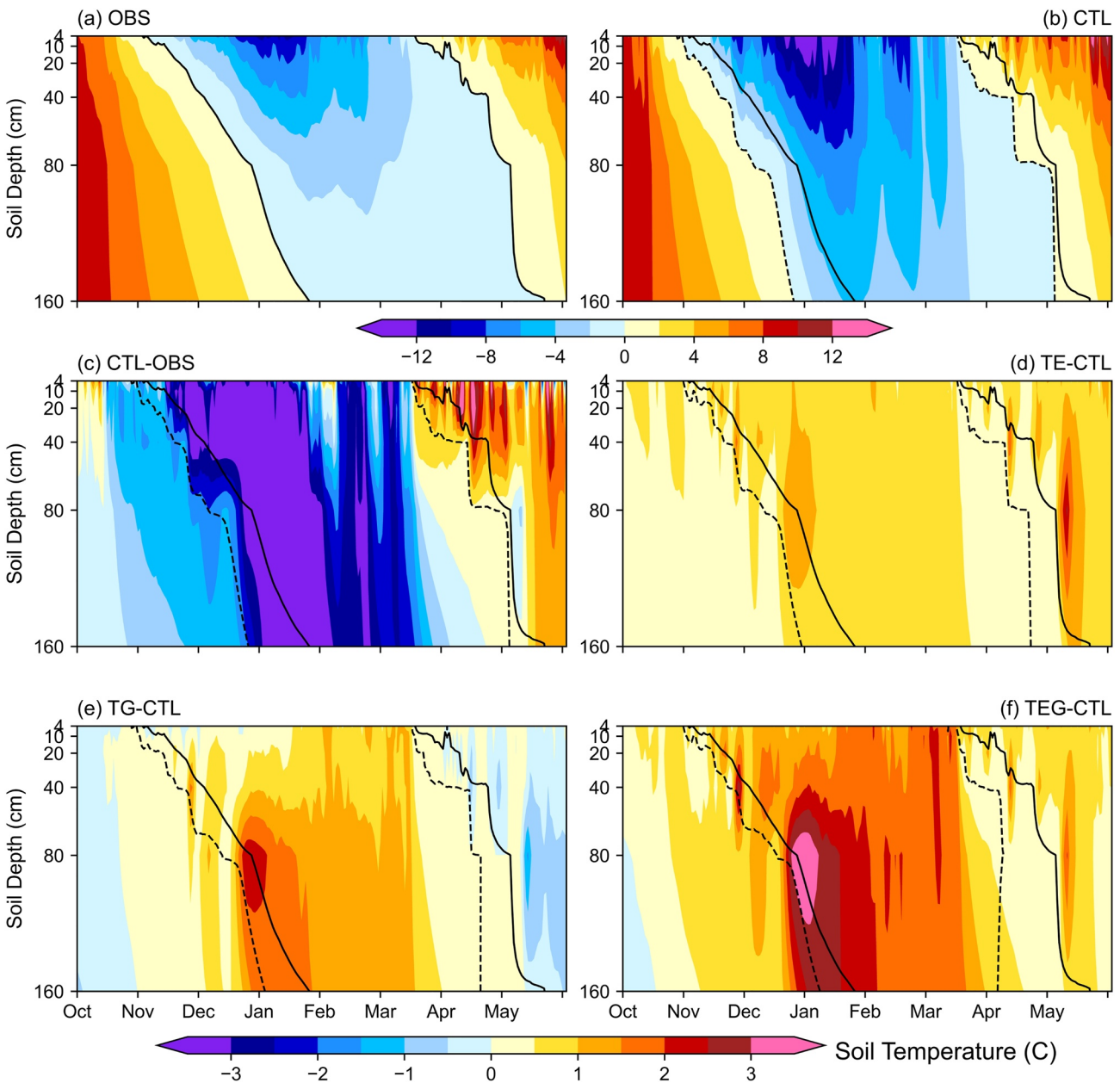


**Figure 7.** The temporal variations of the observed (a) and the CTL experiment simulated (b) daily soil temperature vertical profile and their difference (c) at Arou site during 1 October 2013 to 31 May 2014. And the differences of the simulated soil temperature between each sensitive experiment and CTL experiment (d–f). The black line outlines the freezing and thawing fronts, that is, 0°C isotherm. The solid lines show the observations and the dashed lines show simulations.

–1.63°C and April–May with a bias of –1.67°C. The difference feature between each sensitive experiment and CTL experiment (Figures 8d–8f) at Maqu site is fairly consistent with that at Arou site but with relatively lower values because of the lower increase in VE and lower gravel content. The TEG experiment (Figure 8f) still shows the best simulation of the freezing front among the four experiments.

#### 4.4. The Changes in Regional Soil Temperature Simulation Induced by Adopting the VE and GH Schemes

From Figures 9a and 9b, the CLM5.0 model can produce the same spatial distribution feature of soil temperature as CLDAS over the TP. The soil temperature is much higher in the seasonally frozen soil area than in the permafrost area. However, the CLM5.0 model also mainly shows an underestimation, especially in the southeast part of the TP

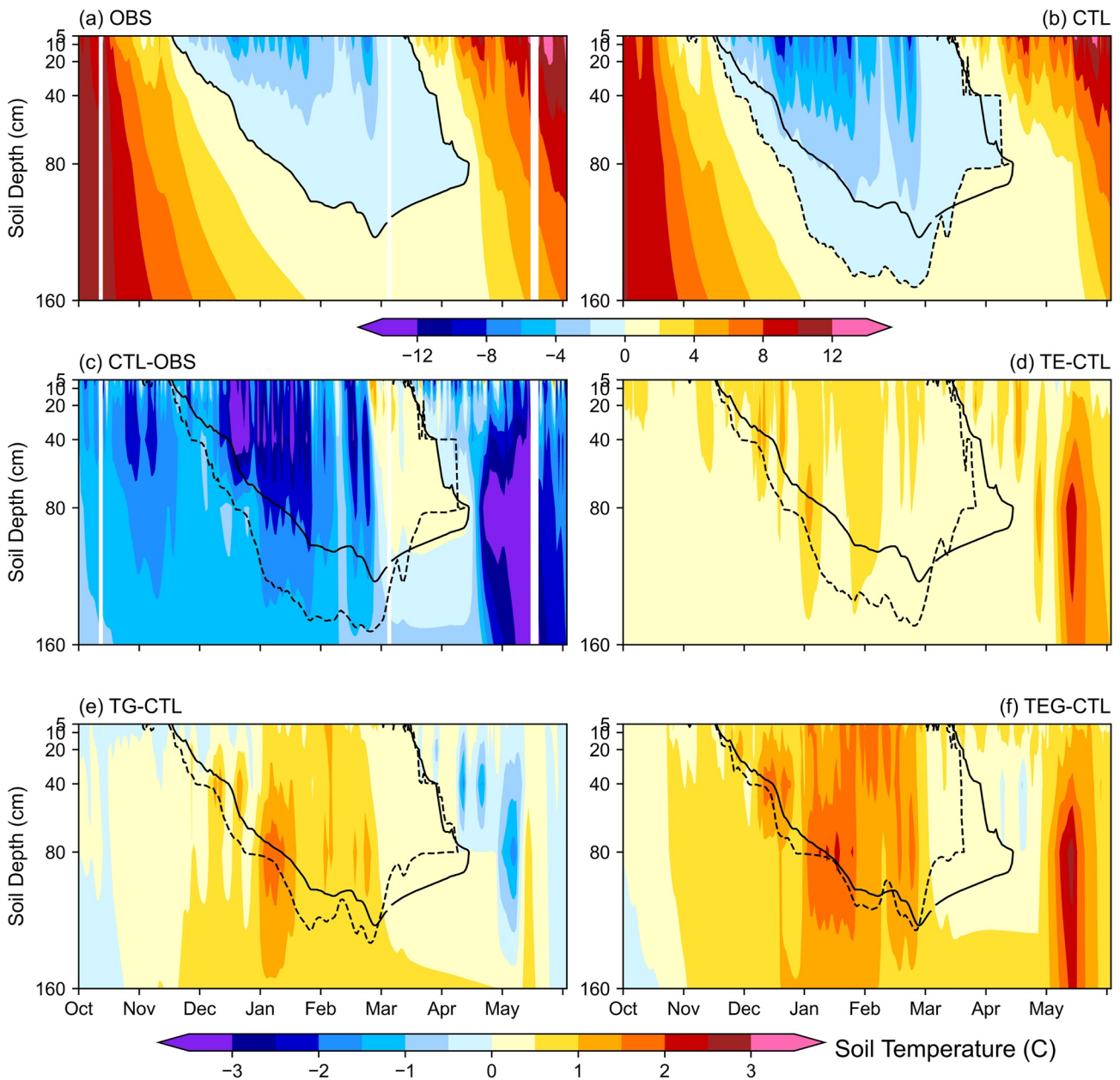
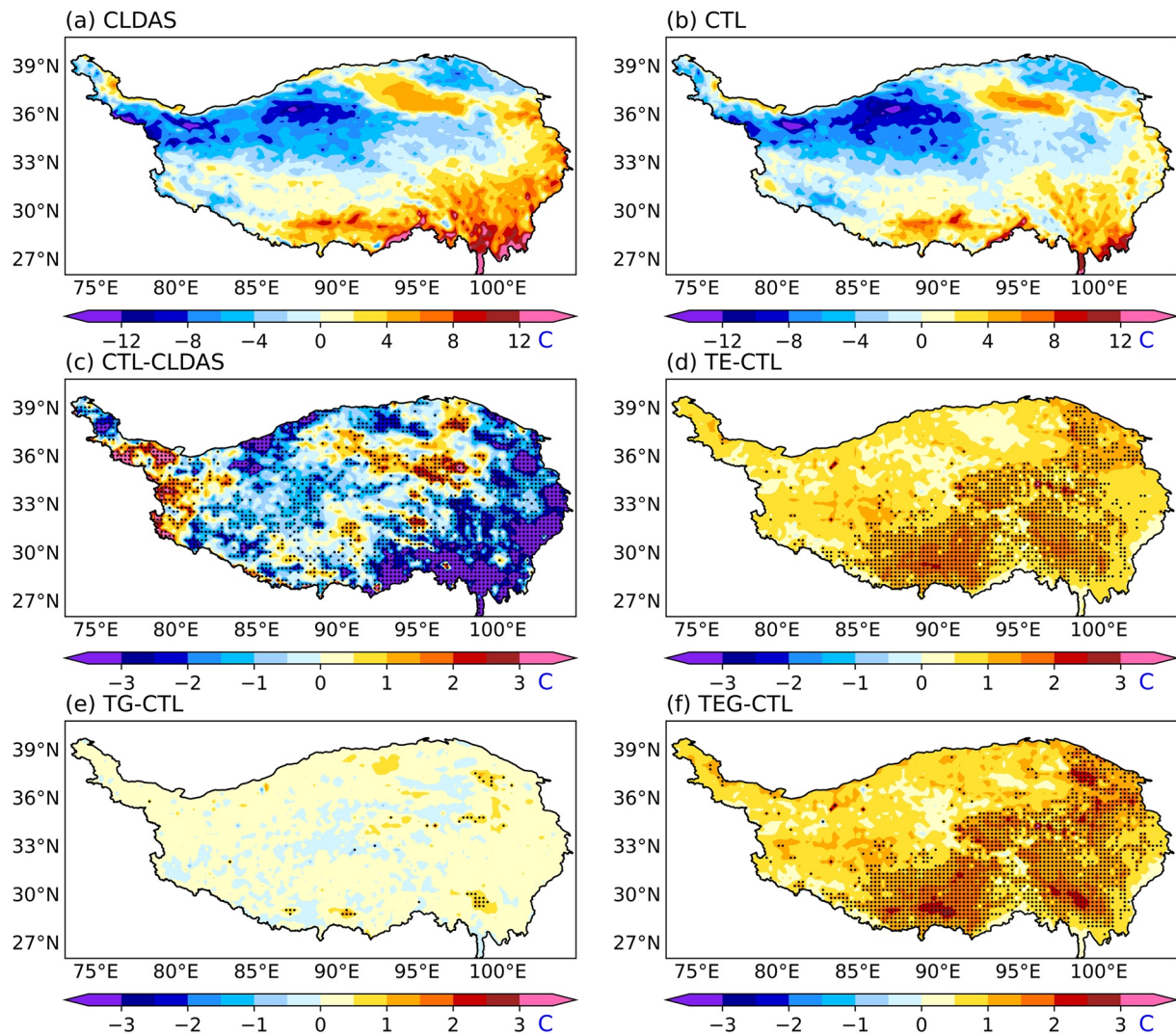


Figure 8. Same as Figure 7, but for Maqu site.

with a relatively heavier vegetation (Figure 9c). But the western part of the TP and the southern edge of the Qaidam Basin where are barely vegetated show an evident overestimation. This could be attributed to the complex topography (Figure 1g), which overestimates the downward surface shortwave radiation (Gu et al., 2022; Huang et al., 2022; X. D. Zhang et al., 2022). The adoption of the VE and GH schemes can both increase the modeled soil temperature (Figures 9d and 9e). The areas of significantly increased soil temperature in the TE experiment correspond well to the distribution of LAI (Figure 1a). Compared to the TE experiment, the TG experiment shows a relatively smaller increased soil temperature with a weak significance. This indicates that the improvement of frozen soil temperature is limited if the surface radiation transfer process affected by the subgrid terrain is omitted, even though the hydro-thermal properties within the soil are revised. Same as the single-point simulation, the TEG experiment with both VE and GH schemes adopted produces a further increased soil temperature and an enhanced significance (Figure 9f).

Figures 10 and 11 give the time–depth distribution of the observed and simulated soil temperature in the regional experiments regionally averaged over all in situ sites at the Maqu and Shiquanhe networks, respectively. The CTL



**Figure 9.** The temporal mean (during 1 October 2013 to 31 May 2014) observed (a) and CTL experiment simulated (b) soil temperature vertically averaged at the depths from 5 to 40 cm and their difference (c) over the Tibetan Plateau. And the differences of the simulated soil temperature between each sensitive experiment and CTL experiment (d–f). The black dots in panels (c)–(f) indicate the significant level above 95% of *t* test.

experiments at Maqu and Shiquanhe networks exhibit cold biases in the freezing and completely frozen periods and warm bias in the thawing period (Figures 10c and 11c). The TE experiment (Figures 10d and 11d) increases the modeled soil temperature during freeze–thaw period while the TG experiment (Figures 10e and 11e) increases (decreases) the modeled soil temperature in the completely frozen period (freezing and thawing periods) at both Maqu and Shiquanhe networks. The changes in soil temperature in the TEG experiment are the quasilinear superposition of the changes in the TE and TG experiments relative to the CTL experiment at both Maqu and Shiquanhe networks too (Figures 10f and 11f). Those are consistent with the findings of the single-point simulations.

#### 4.5. Overall Evaluation of Soil Temperature Simulation Induced by Adopting the VE and GH Schemes

Figure 12 depicts the RMSE and TS of the modeled soil temperature at six soil layers of Arou and Maqu sites produced by CLM5.0 model against the observation. The CLM5.0 model has a better performance in modeling the soil temperature at Maqu site than at Arou site in terms of RMSE and TS, and the column-averaged RMSE (TS) of modeled soil temperature in the CTL experiment are 2.34°C and 1.79°C (0.91 and 0.98) at Arou and Maqu sites, respectively. From Figures 13a and 13c, it is noted that the VE and GH schemes can noticeably improve the soil temperature simulation in terms of RMSE and TS, and the improvements of modeled soil temperature increase with depth because the gravel content and cold bias are higher in the deep layers relative to the upper layers (Figures 2a

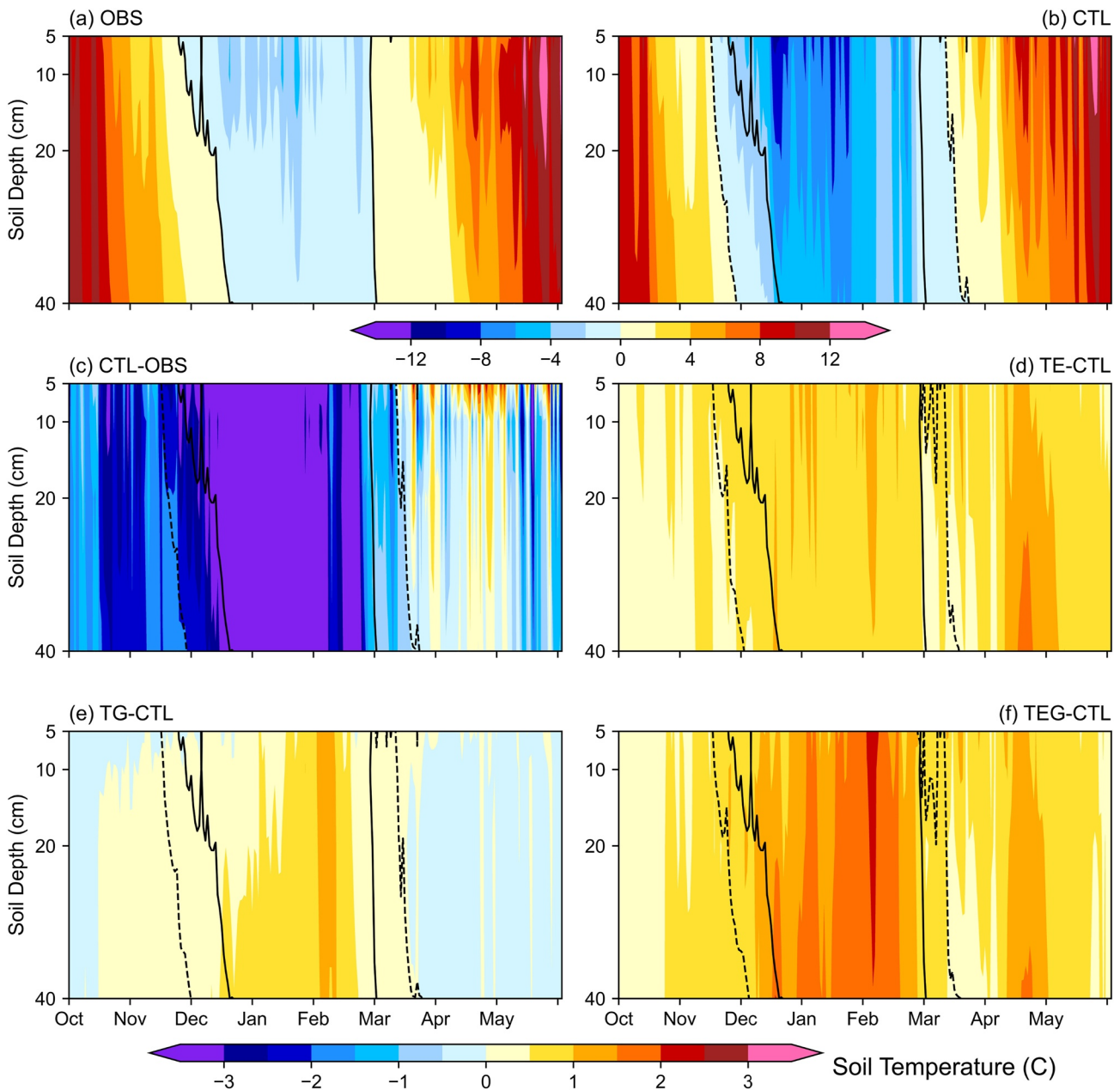


**Figure 10.** Same as Figure 7, but for the soil temperature at different depths regionally averaged over the in situ sites in the Maqu network.

and 14a). The main improvements of simulation skill in soil temperature for both TE, TG, and TEG experiments are located in the freezing and completely frozen periods (Figures 14a–14d). Compared to the CTL experiment with original CLM5.0 model, the column-averaged RMSE (TS) of modeled soil temperature in the TE, TG, and TEG experiments are reduced (increased) by 12.88%, 20.68%, and 31.11% (0.81%, 3.83%, and 4.52%) at Arou site, respectively.

The TE experiment shows much higher skill in simulating the soil temperature than the TG experiment at Maqu site (Figures 13b and 13d) because it is more effective in reducing the cold bias in the freezing and thawing periods (Figures 14f and 14h). Compared to the CTL experiment, the column-averaged RMSE (TS) of modeled soil temperature in the TE, TG, and TEG experiments are reduced (increased) by 25.03%, 10.15%, and 36.87% (0.40%, –0.53%, and 0.04%) at Maqu site, respectively.

In the regional simulations, the modeled soil temperature with the TS is larger than 0.90 (0.99) at Maqu network (Shiquanhe network and the whole TP; Figures 15b, 15d, and 15f). Thus, the relative changes in TS for the



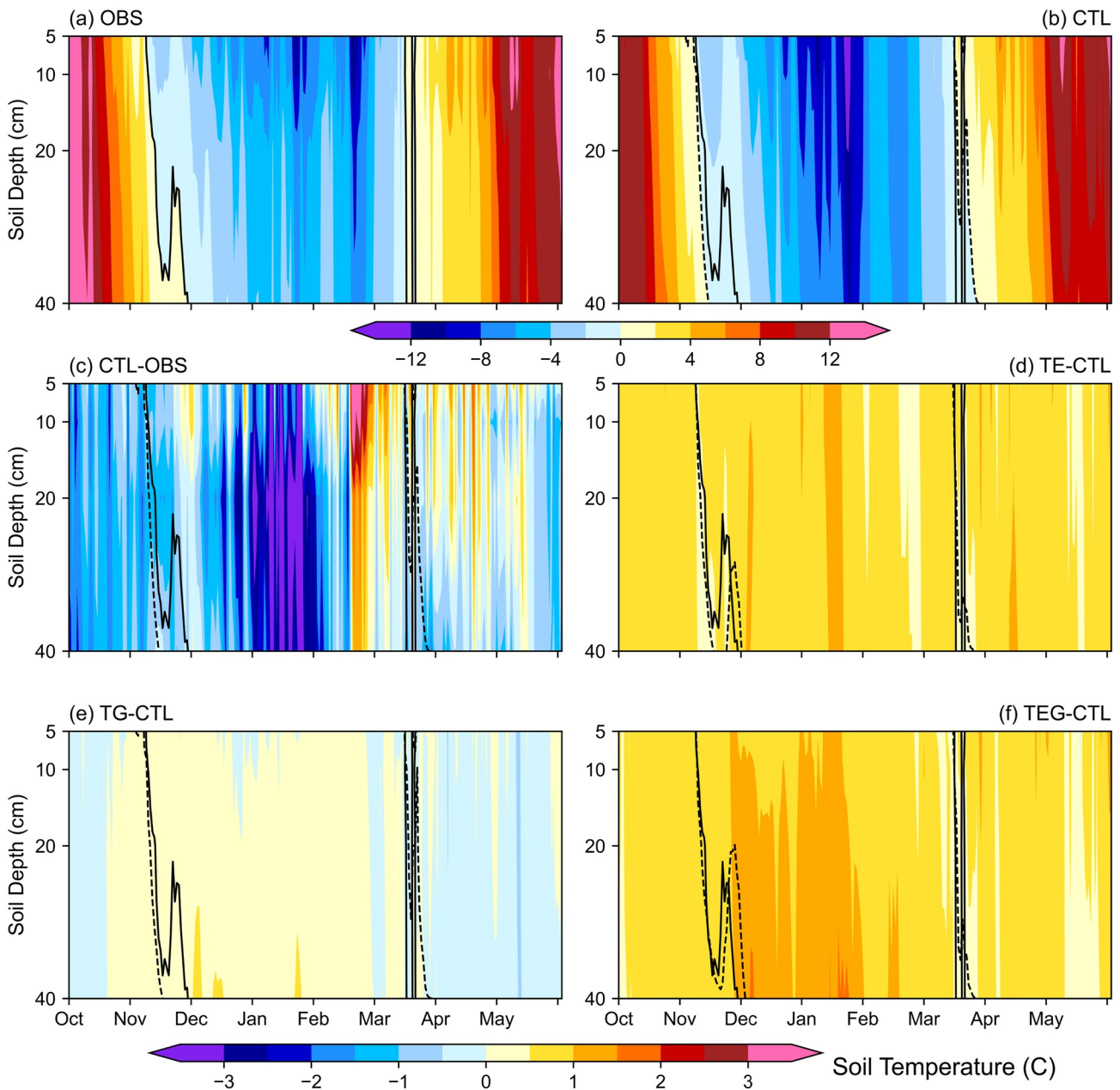
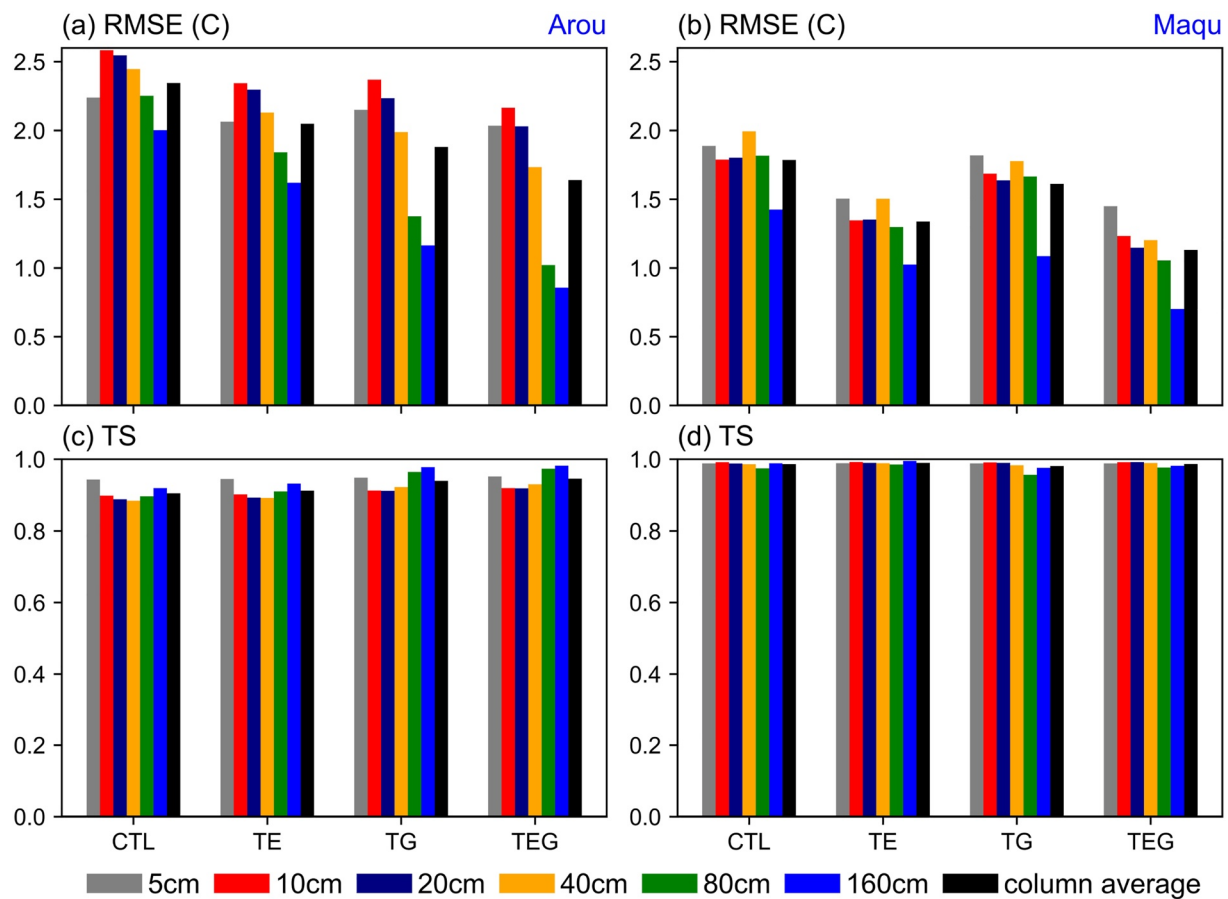


Figure 11. Same as Figure 10, but for the Shiquanhe network.

simulations of soil temperature against observations between each sensitive experiment and CTL experiment are very slight at the two networks and the whole TP (Figures 16b, 16d, and 16f). Meanwhile, the TE experiment performs better to reduce the cold bias of the soil temperature modeled by the CTL experiment than the TG experiment in the regional simulation (Figures 9d and 9e), so the RMSE of modeled soil temperature reduces more in the TE experiment than in the TG experiment relative to the CTL experiment at the two networks and the whole TP (Figures 16a, 16c, and 16e). Compared to the CTL experiment, the column-averaged RMSE (TS) of modeled soil temperature in the TE, TG, and TEG experiments are reduced (increased) by 18.21%, 9.62%, and 27.34% (0.26%, 1.92%, and 2.10%) at Maqu network, by 17.97%, 2.94%, and 20.0% (0.11%, 0.10%, and 0.18%) at Shiquanhe network, and by 32.34%, 6.75%, and 30.18% (0.05%, -0.13%, and -0.07%) over the whole TP, respectively.



**Figure 12.** The root-mean-square error (RMSE) and TS for the simulations of soil temperature at different soil depths in Arou and Maqu sites from each experiment against observations during 1 October 2013 to 31 May 2014.

## 5. Discussion and Conclusion

Frozen soil is an important and typical underlying surface over the TP, but previous studies focus on evaluating the performance of CLM5.0 in simulating the soil temperature and moisture in warm seasons (Deng et al., 2020, 2021; Yuan et al., 2021). The description of the hydrothermal process either at the soil surface or within the soil plays important roles in the soil temperature simulation during freeze–thaw period. This study implemented an improved VE scheme and GH scheme into CLM5.0 model and indicated how the VE and GH schemes affected the model performance. Figure 17 gives the schematic illustration for the effects of the VE and GH schemes on the soil temperature simulation during the freeze–thaw period as follows.

The original CLM5.0 model produces much lower VE than the observation, which can be realistically simulated by adopting the improved VE scheme. Compared to the CTL experiment with original CLM5.0 model, the much higher VE produced by the CLM5.0 model adopting the improved VE scheme in TE experiment leads to more downward long-wave radiation from the vegetation and thereafter less surface upward net long-wave radiation, which results in more surface net radiation (Figure 17a) and thereafter warmer soil temperature at surface and deep layers (Figure 14).

Compared to the CTL experiment with the original CLM5.0 model, the TG experiment with the GH scheme altered the soil heat–water transfer processes by increasing (decreasing) the soil mineral hydrothermal properties of B exponent, bulk density, dry thermal conductivity, and solid heat capacity (the porosity, saturated hydraulic conductivity, saturated matric potential, and solid thermal conductivity). The less heat loss from the soil leads to warmer soil temperature simulated by the TG experiment (Figure 17b), resulting in the cold bias during most time of the freezing and completely frozen periods produced by the CTL experiment significantly reduced.

Overall, the TEG experiment with the improved VE and GH schemes can remarkably reduce the cold bias during the freezing and completely frozen periods produced by the original CLM5.0 model and enhance the ability in

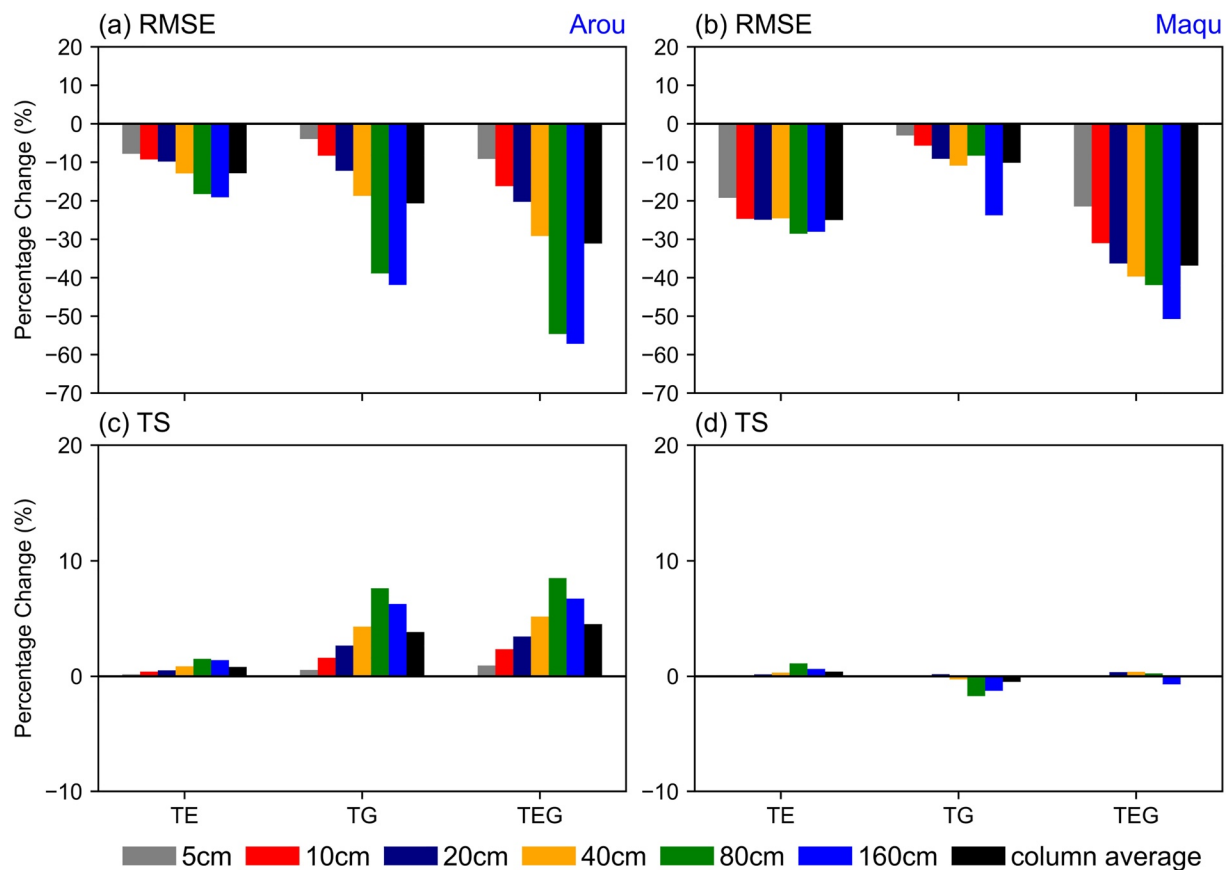


**Figure 13.** The relative changes of root-mean-square error (RMSE) and TS for the simulations of soil temperature at different soil depths at Arou and Maqu sites during 1 October 2013 to 31 May 2014 against observations between each sensitive experiment and CTL experiment.

simulating the soil temperature. However, adopting the improved VE and GH schemes shows much less improvement of the soil moisture simulation relative to the soil temperature and obvious inconsistency at different sites (not shown). This suggests that the processes related to the soil moisture are much more complex than the soil temperature and need to be further revealed and studied in the future work, such as the presence of macropores in the frozen soil (Hansson et al., 2004; Lundberg et al., 2016; Niu et al., 2011).

The forming of macropores during the freeze–thaw period is a distinctive hydrological effect of the frozen soil (Iwata et al., 2010; Laudon et al., 2007; Mohammed et al., 2018). It allows infiltration and water flow achieve within the frozen soil. The ice content within the frozen soil hinders the infiltration and favors the surface runoff. When the daily soil surface freeze–thaw cycle occurs, the snow melt water can even form an almost impermeable “concrete frozen layer” between the ground surface and the snow layer (Ala-Aho et al., 2021). Land surface models always simulate unreasonable hydrological processes in the frozen soil due to the neglect of the macropores (Lundberg et al., 2016; Niu et al., 2011). Niu and Yang (2006) proposed a frozen soil parameterization scheme in CLM2.0, assuming the existence of a partially permeable area, and represented the movement of liquid water through the air-filled macropores and unfrozen pores. Furthermore, Mohammed et al. (2021) developed a dual permeability model based on Darcy’s law, with one domain for slow matrix flow and another for rapid flow through macropore channels, and improved the interaction of infiltration and runoff in structured soils. However, neither the default CLM5.0 model nor the two parameterization schemes adopted in this study involve the presence of macropores in the frozen soil. Besides, although the hydrothermal properties of different soil types vary considerably, soil type is unlikely to be a decisive factor affecting the frozen soil hydrological effect (Ala-Aho et al., 2021; Mustamo et al., 2019).

In addition, previous studies on frozen soil modeling mainly focus on the hydrothermal process within the soil (S. Q. Luo et al., 2008, 2017; C. H. Wang & Yang, 2018), but the hydrothermal process above the soil is equally critical. Although the ability of CLM5.0 model in simulating the soil temperature has been obviously improved in

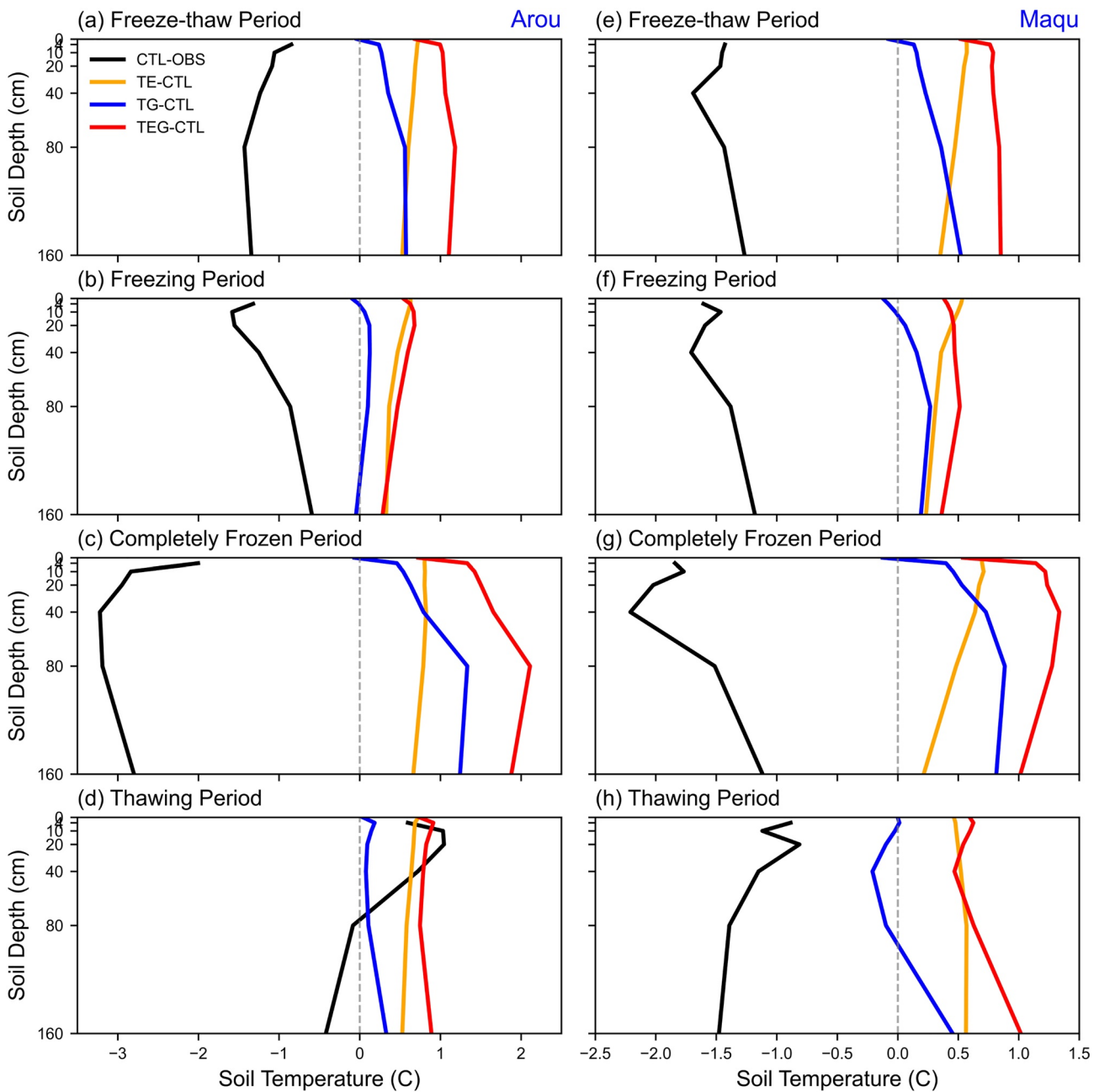


**Figure 14.** The differences of modeled soil temperature between CTL experiment and observation and between each sensitive experiment and CTL experiment at different depths in Arou and Maqu sites averaged over the freeze–thaw period during 1 October 2013 to 31 May 2014.

this study, the snow accumulation process, especially thick snow, was not considered. Snow cover is the dominant land cover during the soil freeze–thaw period and largely determines the spatial distribution of frozen soil (Li et al., 2021; J. X. Luo et al., 2021; S. Q. Luo et al., 2020; Xie et al., 2017). Meanwhile, implementing the subgrid terrain solar radiative effect parameterization scheme into land surface model can produce a more realistic surface heat source and sink (Gu et al., 2022; Huang et al., 2022; X. D. Zhang et al., 2022). These issues still deserve attention in the future work.

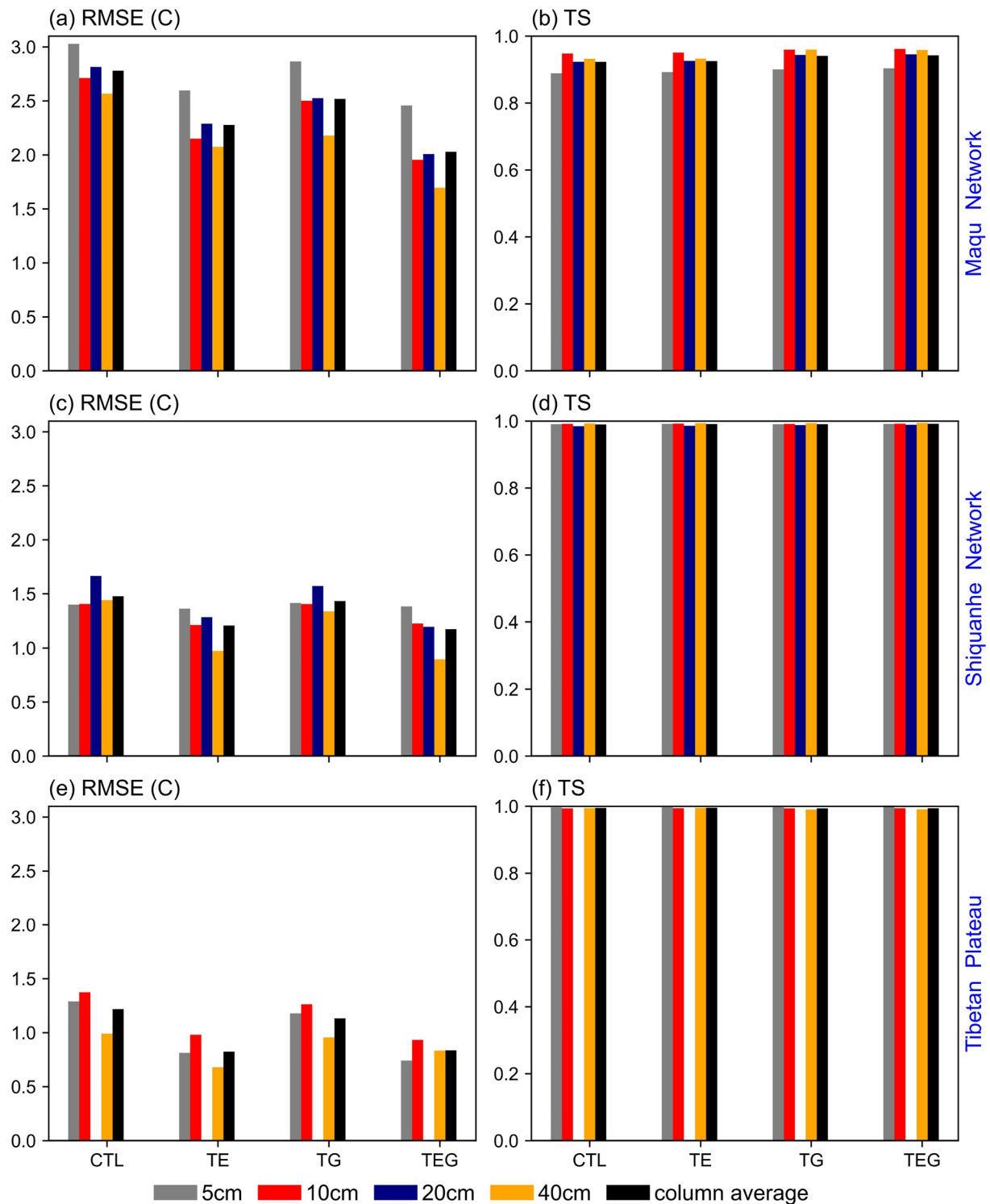


Figure 15. Same as Figure 12, but for the regional simulations.

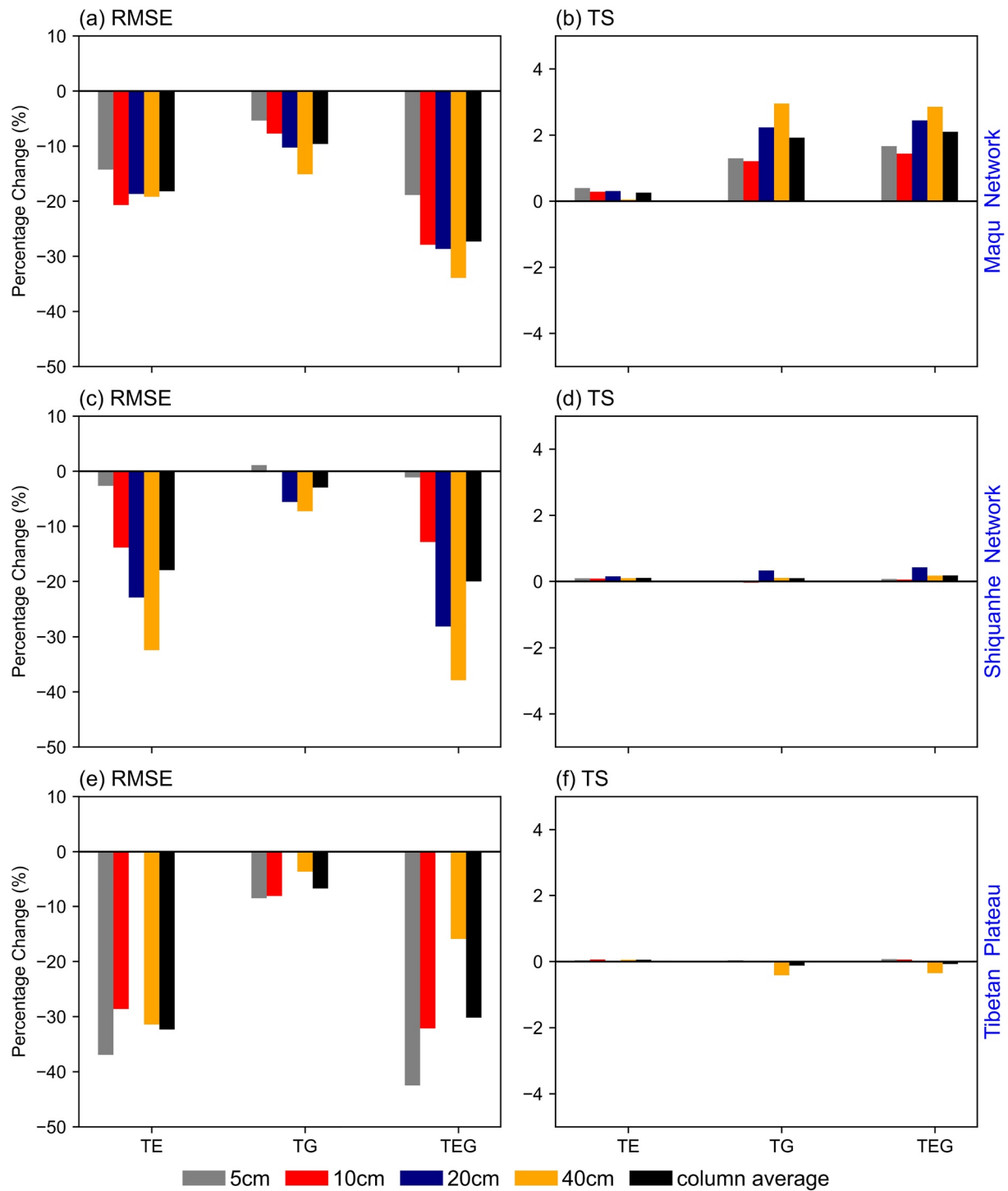
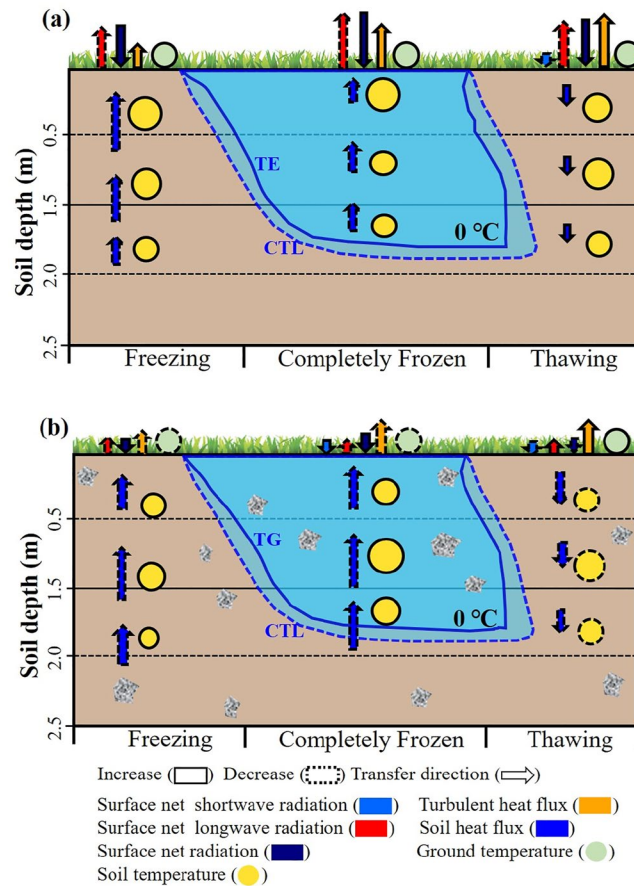


Figure 16. Same as Figure 13, but for the regional simulations.



**Figure 17.** Schematic illustration for the effects of the vegetation emissivity (VE; a) and gravel hydrothermal (GH; b) schemes on soil temperature simulation. The different size represents the change intensity. The blue dashed (solid) line indicates the freezing and thawing fronts simulated by the CTL (TE/TG) experiment.

## Data Availability Statement

The observed data at Arou site (Che et al., 2019) and the model forcing data (J. He et al., 2020) are provided by the Institute of Tibetan Plateau Research, Chinese Academy of Sciences. The observation data at Maqu site (S. Y. Wang, 2016) are from the National Cryosphere Desert Data Center. The observed soil temperature in the Maqu and Shiquanhe networks is derived from P. Zhang et al. (2022). The CLDAS soil temperature (Shi et al., 2011) is provided by the China Meteorological Data Service Center. The Moderate Resolution Imaging Spectroradiometer (MODIS) emissivity products (MOD11A2, version 6.1; Z. Wan et al., 2021) and leaf area index products (MOD15A2H, version 6.1; Myneni et al., 2021) are available at <https://search.earthdata.nasa.gov>. The terrain elevation data with the horizontal resolution of 3" (~90 m; Jarvis et al., 2008) are from [https://developers.google.com/earth-engine/datasets/catalog/CGIAR\\_SRTM90\\_V4](https://developers.google.com/earth-engine/datasets/catalog/CGIAR_SRTM90_V4). The CLM5.0 model is freely available at <http://www.cesm.ucar.edu/models/>.

## References

- Akerman, H. J., & Johansson, M. (2008). Thawing permafrost and thicker active layers in sub-Arctic Sweden. *Permafrost and Periglacial Processes*, 19(3), 279–292. <https://doi.org/10.1002/ppp.626>
- Ala-Aho, P., Autio, A., Bhattacharjee, J., Isokangas, E., Kujala, K., Marttila, H., et al. (2021). What conditions favor the influence of seasonally frozen ground on hydrological partitioning? A systematic review. *Environmental Research Letters*, 16(4), 043008. <https://doi.org/10.1088/1748-9326/abe82c>
- Arocena, J., Hall, K., & Zhu, L. P. (2012). Soil formation in high elevation and permafrost areas in the Qinghai Plateau (China). *Spanish Journal of Soil Science*, 2(2), 34–49. <https://doi.org/10.3232/sjss.2012.v2.n2.02>
- Biskaborn, B. K., Smith, S. L., Noetzi, J., Matthes, H., Vieira, G., Streletskiy, D. A., et al. (2019). Permafrost is warming at a global scale. *Nature Communications*, 10(1), 264.

## Acknowledgments

This study is supported by the National Natural Science Foundation of China under Grant 41975081, the CAS “Light of West China” Program (E129030101, Y929641001), Open Research Fund Program of Plateau Atmosphere and Environment Key Laboratory of Sichuan Province (PAEKL-2023-K01), the Jiangsu University “Blue Project” Outstanding Young Teachers Training Object, and the Jiangsu Collaborative Innovation Center for Climate Change. We are grateful to NCAR for its open-source policy and for allowing us to use CLM5.0 model. We appreciate the three anonymous reviewers for their constructive suggestions to greatly improve the manuscript.

- Che, T., Li, L., Liu, S. M., Li, H. Y., Xu, Z. W., Tan, J. L., et al. (2019). Integrated hydrometeorological, snow and frozen-ground observations in the alpine region of the Heihe River Basin, China. *Earth System Science Data*, *11*(3), 1483–1499. <https://doi.org/10.5194/essd-11-1483-2019>
- Chen, Y. Y., Yang, K., Tang, W. J., Qin, J., & Zhao, L. (2012). Parameterizing soil organic carbon's impacts on soil porosity and thermal parameters for Eastern Tibet grasslands. *Science China Earth Sciences*, *55*(6), 1001–1011. <https://doi.org/10.1007/s11430-012-4433-0>
- Côté, J., & Konrad, J. M. (2005). A generalized thermal conductivity model for soils and construction materials. *Canadian Geotechnical Journal*, *42*(2), 443–458. <https://doi.org/10.1139/t04-106>
- Cousin, I., Nicoullaud, B., & Coutadeur, C. (2003). Influence of rock fragments on the water retention and water percolation in a calcareous soil. *Catena*, *53*(2), 97–114. [https://doi.org/10.1016/s0341-8162\(03\)00037-7](https://doi.org/10.1016/s0341-8162(03)00037-7)
- Dai, Y. J., Zeng, X. B., Dickinson, R. E., Baker, I., Bonan, G. B., Bosilovich, M. G., et al. (2003). The Common Land Model. *Bulletin of the American Meteorological Society*, *84*(8), 1013–1024. <https://doi.org/10.1175/bams-84-8-1013>
- Deng, M. S., Meng, X. H., Lu, Y. Q., Li, Z. G., Zhao, L., Hu, Z. Y., et al. (2021). Impact and sensitivity analysis of soil water and heat transfer parameterizations in Community Land Surface Model on the Tibetan Plateau. *Journal of Advances in Modeling Earth Systems*, *13*, e2021MS002670. <https://doi.org/10.1029/2021MS002670>
- Deng, M. S., Meng, X. H., Lyu, Y. Q., Zhao, L., Li, Z. G., Hu, Z. Y., & Jing, H. (2020). Comparison of soil water and heat transfer modeling over the Tibetan Plateau using two community land surface model (CLM) versions. *Journal of Advances in Modeling Earth Systems*, *12*, e2020MS002189. <https://doi.org/10.1029/2020MS002189>
- Elberling, B., Michelsen, A., Schadel, C., Schuur, E. A. G., Christiansen, H. H., Berg, L., et al. (2013). Long-term CO<sub>2</sub> production following permafrost thaw. *Nature Climate Change*, *3*(10), 890–894. <https://doi.org/10.1038/nclimate1955>
- Fu, C. W., Hu, Z. Y., Lu, S., Wu, D., & Fan, W. W. (2022). A simulation study on soil parameterization scheme of seasonally frozen ground regions based on CLM4.5. *Plateau Meteorology*, *41*(1), 93–106.
- Gao, R., Wei, Z. G., Dong, W. J., & Hailing, Z. (2005). Impact of the anomalous thawing in the Tibetan Plateau on summer precipitation in China and its mechanism. *Advances in Atmospheric Sciences*, *22*(2), 238–245. <https://doi.org/10.1007/bf02918513>
- Gu, C. L., Huang, A. N., Zhang, Y. C., Yang, B., Cai, S. X., Xu, X. K., et al. (2022). The wet bias of RegCM4 over Tibet Plateau in summer reduced by adopting the 3D sub-grid terrain solar radiative effect parameterization scheme. *Journal of Geophysical Research: Atmospheres*, *127*, e2022JD037434. <https://doi.org/10.1029/2022JD037434>
- Guo, D. L., & Wang, H. J. (2013). Simulation of permafrost and seasonally frozen ground conditions on the Tibetan Plateau, 1981–2010. *Journal of Geophysical Research: Atmospheres*, *118*, 5216–5230. <https://doi.org/10.1002/jgrd.50457>
- Guo, D. L., & Wang, H. J. (2016). CMIP5 permafrost degradation projection: A comparison among different regions. *Journal of Geophysical Research: Atmospheres*, *121*, 4499–4517. <https://doi.org/10.1002/2015JD024108>
- Guo, D. L., & Wang, H. J. (2017a). Permafrost degradation and associated ground settlement estimation under 2°C global warming. *Climate Dynamics*, *49*(7), 2569–2583. <https://doi.org/10.1007/s00382-016-3469-9>
- Guo, D. L., & Wang, H. J. (2017b). Simulated historical (1901–2010) changes in the permafrost extent and active layer thickness in the Northern Hemisphere. *Journal of Geophysical Research: Atmospheres*, *122*, 12285–12295. <https://doi.org/10.1002/2017JD027691>
- Guo, G. L., Yang, M. X., & Wang, H. J. (2011). Sensible and latent heat flux response to diurnal variation in soil surface temperature and moisture under different freeze/thaw soil conditions in the seasonal frozen soil region of the central Tibetan Plateau. *Environmental Earth Sciences*, *63*(1), 97–107. <https://doi.org/10.1007/s12665-010-0672-6>
- Hansson, K., Šimůnek, J., Mizoguchi, M., Lundin, L. C., & Van Genuchten, M. T. (2004). Water flow and heat transport in frozen soil: Numerical solution and freeze–thaw applications. *Vadose Zone Journal*, *3*(2), 693–704. <https://doi.org/10.2113/3.2.693>
- He, H. L., He, D., Jin, J. M., Smits, K. M., Dyck, M., Wu, Q. B., et al. (2020). Room for improvement: A review and evaluation of 24 soil thermal conductivity parameterization schemes commonly used in land-surface, hydrological, and soil–vegetation–atmosphere transfer models. *Earth-Science Reviews*, *211*, 103419. <https://doi.org/10.1016/j.earscirev.2020.103419>
- He, J., Yang, K., Tang, W., Lu, H., Qin, J., Chen, Y. Y., & Li, X. (2020). The first high-resolution meteorological forcing dataset for land process studies over China. *Scientific Data*, *7*(1), 25. <https://doi.org/10.1038/s41597-020-0369-y>
- Huang, A. N., Gu, C. L., Zhang, Y. C., Li, W. P., Zhang, L. J., Wu, Y., et al. (2022). Development of a clear-sky 3D sub-grid terrain solar radiative effect parameterization scheme based on the mountain radiation theory. *Journal of Geophysical Research: Atmospheres*, *127*, e2022JD036449. <https://doi.org/10.1029/2022JD036449>
- Huang, A. N., Lazhu, Wang, J. B., Dai, Y. J., Yang, K., Wei, N., et al. (2019). Evaluating and improving the performance of three 1-D Lake models in a large deep lake of the central Tibetan Plateau. *Journal of Geophysical Research: Atmospheres*, *124*, 3143–3167. <https://doi.org/10.1029/2018JD029610>
- Huang, A. N., Zhao, Y., Zhou, Y., Yang, B., Zhang, L. J., Dong, X. N., et al. (2016). Evaluation of multi-satellite precipitation products by use of ground-based data over China. *Journal of Geophysical Research: Atmospheres*, *121*, 10654–10675. <https://doi.org/10.1002/2016JD025456>
- Iwata, Y., Hayashi, M., Suzuki, S., Hirota, T., & Hasegawa, S. (2010). Effects of snow cover on soil freezing, water movement, and snowmelt infiltration: A paired plot experiment. *Water Resources Research*, *46*, W09504. <https://doi.org/10.1029/2009WR008070>
- Jarvis, A., Reuter, H. I., Nelson, A., & Guevara, E. (2008). The Shuttle Radar Topography Mission (SRTM) 90 m Digital Elevation Database v4.1 [Dataset]. International Centre for Tropical Agriculture (CIAT). Retrieved from [https://developers.google.com/earth-engine/datasets/catalog/CGIAR\\_SRTM90\\_V4](https://developers.google.com/earth-engine/datasets/catalog/CGIAR_SRTM90_V4)
- Jin, H. J., Li, S. X., Cheng, G. D., Shaoling, W., & Li, X. (2000). Permafrost and climatic change in China. *Global and Planetary Change*, *26*(4), 387–404. [https://doi.org/10.1016/s0921-8181\(00\)00051-5](https://doi.org/10.1016/s0921-8181(00)00051-5)
- Jin, M. L., & Liang, S. L. (2006). An improved land surface emissivity parameter for land surface models using global remote sensing observations. *Journal of Climate*, *19*(12), 2867–2881. <https://doi.org/10.1175/JCLI3720.1>
- Laudon, H., Sjöblom, V., Buffam, I., Seibert, J., & Mörth, M. (2007). The role of catchment scale and landscape characteristics for runoff generation of boreal streams. *Journal of Hydrology*, *344*(3–4), 198–209. <https://doi.org/10.1016/j.jhydrol.2007.07.010>
- Lawrence, D. M., Fisher, R. A., Koven, C. D., Oleson, K. W., Swenson, S. C., Bonan, G., et al. (2019). The Community Land Model version 5: Description of new features, benchmarking, and impact of forcing uncertainty. *Journal of Advances in Modeling Earth Systems*, *11*, 4245–4287. <https://doi.org/10.1029/2018MS001583>
- Lawrence, D. M., & Slater, A. G. (2008). Incorporating organic soil into a global climate model. *Climate Dynamics*, *30*(2–3), 145–160. <https://doi.org/10.1007/s00382-007-0278-1>
- Lawrence, D. M., Slater, A. G., & Swenson, S. C. (2012). Simulation of present-day and future permafrost and seasonally frozen ground conditions in CCSM4. *Journal of Climate*, *25*(7), 2207–2225. <https://doi.org/10.1175/JCLI-D-11-00334.1>
- Li, T., Chen, Y. Z., Han, L. J., Cheng, L. H., Lv, Y. H., Fu, B. J., et al. (2021). Shortened duration and reduced area of frozen soil in the Northern Hemisphere. *The Innovation*, *2*(3), 100146. <https://doi.org/10.1016/j.xinn.2021.100146>



- Lin, Z. H., Zeng, Q. C., & Ouyang, B. (1996). Sensitivity of the IAP two-level AGCM to surface albedo variations. *Theoretical and Applied Climatology*, 55(1–4), 157–162. <https://doi.org/10.1007/bf00864711>
- Liu, H. L., Hu, Z. Y., Han, G., & Pei, C. C. (2020). Assessment of freeze–thaw process simulation in Qinghai–Tibetan Plateau by different parameterization schemes based on Noah-MP land surface model. *Plateau Meteorology*, 39(1), 1–14.
- Liu, Y. G., Lyu, S. H., Ma, C. L., Xu, Y., & Luo, J. X. (2021). Gravel parameterization schemes and its regional assessment on Tibetan Plateau using RegCM4. *Journal of Advances in Modeling Earth Systems*, 13, e2020MS002444. <https://doi.org/10.1029/2020MS002444>
- Lundberg, A., Ala-Aho, P., Eklo, O., Klöve, B., Kvarner, J., & Stumpp, C. (2016). Snow and frost: Implications for spatiotemporal infiltration patterns—A review. *Hydrological Processes*, 30(8), 1230–1250. <https://doi.org/10.1002/hyp.10703>
- Luo, J. X., Lyu, S. H., Fang, X. W., & Liu, Y. G. (2021). Trends in the frozen ground temperature on the Tibetan Plateau simulated by RegCM4.7-CLM4.5. *Theoretical and Applied Climatology*, 145(3), 891–901. <https://doi.org/10.1007/s00704-021-03664-3>
- Luo, J. X., Lyu, S. H., Ma, C. L., & Fang, X. W. (2022). Simulation analysis of soil water and heat characteristics in high and low snowfall years on the Qinghai–Xizang Plateau. *Plateau Meteorology*, 41(1), 35–46.
- Luo, S. Q., Chen, B. L., Lyu, S. H., Fang, X. W., Wang, J. Y., Meng, X. H., et al. (2018). An improvement of soil temperature simulations on the Tibetan Plateau. *Sciences in Cold and Arid Regions*, 10(1), 80–94.
- Luo, S. Q., Fang, X. W., Lyu, S. H., Zhang, Y., & Chen, B. L. (2017). Improving CLM4.5 simulations of land–atmosphere exchange during freeze–thaw processes on the Tibetan Plateau. *Journal of Meteorological Research*, 31(5), 916–930. <https://doi.org/10.1007/s13351-017-6063-0>
- Luo, S. Q., Lyu, S. H., & Zhang, Y. (2008). Simulation analysis on the land surface process of BJ site of Central Tibetan Plateau using CoLM. *Plateau Meteorology*, 27, 259–271.
- Luo, S. Q., Wang, J. Y., Pomeroy, J. W., & Lyu, S. H. (2020). Freeze–thaw changes of seasonally frozen ground on the Tibetan Plateau from 1960 to 2014. *Journal of Climate*, 33(21), 9427–9446. <https://doi.org/10.1175/JCLI-D-19-0923.1>
- Ma, C. L., Lyu, S. H., Pan, Y. J., et al. (2020). Impact and sensitivity analysis of gravel parameterization on simulation of land surface processes on the Qinghai–Xizang plateau. *Plateau Meteorology*, 39(6), 1219–1231.
- Ma, X. G., Jin, J. M., Liu, J., & Niu, G. Y. (2019). An improved vegetation emissivity scheme for land surface modeling and its impact on snow cover simulations. *Climate Dynamics*, 53(9–10), 6215–6226. <https://doi.org/10.1007/s00382-019-04924-9>
- Mohammed, A. A., Cey, E. E., Hayashi, M., Callaghan, M. V., Park, Y. J., Miller, K. L., & Frey, S. K. (2021). Dual-permeability modeling of preferential flow and snowmelt partitioning in frozen soils. *Vadose Zone Journal*, 20(2), e20101. <https://doi.org/10.1002/vzj2.20101>
- Mohammed, A. A., Kurylyk, B. L., Cey, E. E., & Hayashi, M. (2018). Snowmelt infiltration and macropore flow in frozen soils: Overview, knowledge gaps, and a conceptual framework. *Vadose Zone Journal*, 17, 1–15. <https://doi.org/10.2136/vzj2018.04.0084>
- Mullens, T. J. (2013). Evaluation and improvements of the offline CLM4 using ARM data (master's thesis). San Jose State University.
- Mustamo, P., Ronkanen, A., Berglund, Ö., Berglund, K., & Klöve, B. (2019). Thermal conductivity of unfrozen and partially frozen managed peat soils. *Soil and Tillage Research*, 191, 245–255. <https://doi.org/10.1016/j.still.2019.02.017>
- Myneni, R., Knyazikhin, Y., & Park, T. (2021). MODIS/Terra Leaf Area Index/FPAR 8-Day L4 Global 500m SIN Grid V061 [Dataset]. NASA EOSDIS Land Processes DAAC. <https://doi.org/10.5067/MODIS/MOD15A2H.061>
- Niu, G. Y., & Yang, Z. L. (2006). Effects of frozen soil on snowmelt runoff and soil water storage at a continental scale. *Journal of Hydrometeorology*, 7(5), 937–952. <https://doi.org/10.1175/jhm538.1>
- Niu, G. Y., Yang, Z. L., Mitchell, K. E., Chen, F., Ek, M. B., Barlage, M., et al. (2011). The community Noah land surface model with multi-parameterization options (Noah-MP): 1. Model description and evaluation with local-scale measurements. *Journal of Geophysical Research*, 116, D12109. <https://doi.org/10.1029/2010jd015139>
- Ogawa, K., Schmugge, T., Jacob, F., & French, A. (2003). Estimation of land surface window (8–12 μm) emissivity from multi-spectral thermal infrared remote sensing—a case study in a part of Sahara Desert. *Geophysical Research Letters*, 30(2), 1067. <https://doi.org/10.1029/2002GL016354>
- Pan, Y. J., Lyu, S. H., & Gao, Y. H. (2015). Simulation of the influence of gravel on soil thermal and hydraulic properties on Qinghai–Xizang Plateau. *Plateau Meteorology*, 34(5), 1224–1236.
- Pan, Y. J., Lyu, S. H., Li, S. S., Gao, Y., Meng, X., Ao, Y., & Wang, S. (2015). Simulating the role of gravel in freeze–thaw process on the Qinghai–Tibet Plateau. *Theoretical and Applied Climatology*, 127(3), 1011–1022. <https://doi.org/10.1007/s00704-015-1684-7>
- Peck, A. J., & Watson, J. D. (1979). *Hydraulic conductivity and flow in non-uniform soil*. CSIRO Division of Environmental Mechanics.
- Peng, X., Zhang, T., Frauenfeld, O. W., Wang, K., Luo, D., Cao, B., et al. (2018). Spatiotemporal changes in active layer thickness under contemporary and projected climate in the Northern Hemisphere. *Journal of Climate*, 31(1), 251–266. <https://doi.org/10.1175/JCLI-D-16-0721.1>
- Poesen, J., & Lavee, H. (1994). Rock fragments in top soils: Significance and processes. *Catena*, 23(2), 1–28. [https://doi.org/10.1016/0341-8162\(94\)90050-7](https://doi.org/10.1016/0341-8162(94)90050-7)
- Ran, Y. H., Li, X., Cheng, G. D., Zhang, T., Wu, Q., Jin, H., & Jin, R. (2012). Distribution of permafrost in China: An overview of existing permafrost maps. *Permafrost and Periglacial Processes*, 23(4), 322–333. <https://doi.org/10.1002/ppp.1756>
- Russo, D. (1983). Leaching characteristics of a stony desert soil. *Soil Science Society of America Journal*, 47(3), 431–438. <https://doi.org/10.2136/sssaj1983.03615995004700030008x>
- Schuur, E. A. G., Bockheim, J., Canadell, J. G., Euskirchen, E., Field, C. B., Goryachkin, S. V., et al. (2008). Vulnerability of permafrost carbon to climate change: Implications for the global carbon cycle. *BioScience*, 58(8), 701–714. <https://doi.org/10.1641/b580807>
- Schuur, E. A. G., McGuire, A. D., Schadel, C., Grosse, G., Harden, J. W., Hayes, D. J., et al. (2015). Climate change and the permafrost carbon feedback. *Nature*, 520(7546), 171–179. <https://doi.org/10.1038/nature14338>
- Shang, L. Y., Zhang, Y., Lyu, S. H., & Wang, S. (2015). Energy exchange of an alpine grassland on the eastern Qinghai–Tibetan Plateau. *Science Bulletin*, 60(4), 435–446. <https://doi.org/10.1007/s11434-014-0685-8>
- Shangguan, W., Dai, Y. J., Duan, Q. Y., Liu, B. Y., & Yuan, H. (2014). A global soil data set for Earth system modeling. *Journal of Advances in Modeling Earth Systems*, 6, 249–263. <https://doi.org/10.1002/2013MS000293>
- Shi, C. X., Xie, Z. H., Qian, H., Liang, M., & Yang, X. (2011). China land soil moisture EnKF data assimilation based on satellite remote sensing data. *Science China Earth Sciences*, 54(9), 1430–1440. <https://doi.org/10.1007/s11430-010-4160-3>
- Su, Y. Q., Zhang, Y., & Song, M. H. (2020). Evaluation of simulated performance of CLM4.5 in Alpine Meadow over the Qinghai–Xizang Plateau based on measured soil properties. *Plateau Meteorology*, 39(6), 1295–1308.
- Taylor, K. E. (2001). Summarizing multiple aspects of model performance in a single diagram. *Journal of Geophysical Research*, 106(D7), 7183–7192. <https://doi.org/10.1029/2000JD900719>
- Ullah, W., Wang, G. J., Gao, Z. Q., Tawia Hagan, D. F., Bhatti, A. S., & Zhua, C. (2021). Observed linkage between Tibetan Plateau soil moisture and South Asian summer precipitation and the possible mechanism. *Journal of Climate*, 34(1), 361–377. <https://doi.org/10.1175/JCLI-D-20-0347.1>
- Vasiliev, A. A., Drozdov, D. S., Gravis, A. G., Malkova, G. V., Nyland, K. E., & Streletskiy, D. A. (2020). Permafrost degradation in the western Russian arctic. *Environmental Research Letters*, 15(4), 045001. <https://doi.org/10.1088/1748-9326/ab6f12>

- Vecellio, D. J., Nowotarski, C. J., & Frauenfeld, O. W. (2019). The role of permafrost in Eurasian land–atmosphere interactions. *Journal of Geophysical Research: Atmospheres*, *124*, 11644–11660. <https://doi.org/10.1029/2019JD031204>
- Wan, Z., Hook, S., & Hulley, G. (2021). MODIS/Terra Land Surface Temperature/Emissivity 8-Day L3 Global 1km SIN Grid V061 [Dataset]. NASA EOSDIS Land Processes DAAC. <https://doi.org/10.5067/MODIS/MOD11A2.061>
- Wan, Z. M. (2014). New refinements and validation of the collection-6 MODIS land-surface temperature/emissivity product. *Remote Sensing of Environment*, *140*, 36–45. <https://doi.org/10.1016/j.rse.2013.08.027>
- Wang, C. H., & Yang, K. (2018). A new scheme for considering soil water-heat transport coupling based on Community Land Model: Model description and preliminary validation. *Journal of Advances in Modeling Earth Systems*, *10*, 927–950. <https://doi.org/10.1002/2017MS001148>
- Wang, C. H., Yang, K., & Zhang, F. M. (2020). Impacts of soil freeze–thaw process and snow melting over Tibetan Plateau on Asian summer Monsoon system: A review and perspective. *Frontiers of Earth Science*, *8*, 133. <https://doi.org/10.3389/feart.2020.00133>
- Wang, J. Y., Luo, S. Q., Li, Z. G., Wang, S. Y., & Li, Z. H. (2019). The freeze/thaw process and the surface energy budget of the seasonally frozen ground in the source region of the Yellow River. *Theoretical and Applied Climatology*, *138*(3–4), 1631–1646. <https://doi.org/10.1007/s00704-019-02917-6>
- Wang, K., Wan, Z., Wang, P., Sparrow, M., Liu, J., & Haginoya, S. (2007). Evaluation and improvement of the MODIS land surface temperature/emissivity products using ground-based measurements at a semi-desert site on the western Tibetan Plateau. *International Journal of Remote Sensing*, *28*(11), 2549–2565. <https://doi.org/10.1080/01431160600702665>
- Wang, S. Y. (2016). *Meteorological tower observation data from the Ruoege Alpine Wetland ecosystem Research Station Maqu Observatory in 2014*. National Glacial and Frozen Desert Scientific Data Center. <https://doi.org/10.12072/casnw.020.2017.db>
- Wang, S. Y., Zhang, Y., Lyu, S. H., Su, P., Shang, L., & Li, Z. (2016). Biophysical regulation of carbon fluxes over an alpine meadow ecosystem in the eastern Tibetan Plateau. *International Journal of Biometeorology*, *60*(6), 801–812. <https://doi.org/10.1007/s00484-015-1074-y>
- Wang, X. J., Ran, Y. H., Pang, G. J., Chen, D., Su, B., Chen, R., et al. (2022). Contrasting characteristics, changes, and linkages of permafrost between the Arctic and the Third Pole. *Earth-Science Reviews*, *230*, 104042. <https://doi.org/10.1016/j.earscirev.2022.104042>
- Wu, Q. B., & Zhang, T. J. (2010). Changes in active layer thickness over the Qinghai–Tibetan Plateau from 1995 to 2007. *Journal of Geophysical Research*, *115*, D09107. <https://doi.org/10.1029/2009JD012974>
- Wu, X. D., Zhao, L., Fang, H. B., Chen, J., Pang, Q. Q., Wang, Z. W., et al. (2012). Soil enzyme activities in permafrost regions of the western Qinghai–Tibetan Plateau. *Soil Science Society of America Journal*, *76*(4), 1280–1289. <https://doi.org/10.2136/sssaj2011.0400>
- Xie, Z. P., Hu, Z. Y., & Liu, H. L. (2017). Evaluation of the surface energy exchange simulations of land surface model CLM 4.5 in the alpine meadow over the Qinghai–Xizang Plateau. *Plateau Meteorology*, *36*(1), 1–12.
- Xie, Z. P., Hu, Z. Y., Ma, Y. M., Sun, G. H., Gu, L. L., Liu, S., et al. (2019). Modeling blowing snow over the Tibetan Plateau with the Community Land Model: Method and preliminary evaluation. *Journal of Geophysical Research: Atmospheres*, *124*, 9332–9355. <https://doi.org/10.1029/2019JD030684>
- Yang, K., & Wang, C. H. (2019a). Seasonal persistence of soil moisture anomalies related to freeze–thaw over the Tibetan Plateau and prediction signal of summer precipitation in eastern China. *Climate Dynamics*, *53*(3–4), 2411–2424. <https://doi.org/10.1007/s00382-019-04867-1>
- Yang, K., & Wang, C. H. (2019b). Water storage effect of soil freeze–thaw process and its impacts on soil hydro-thermal regime variations. *Agricultural and Forest Meteorology*, *265*, 280–294. <https://doi.org/10.1016/j.agrformet.2018.11.011>
- Yang, K., Wu, H., Qin, J., Lin, C., Tang, W., & Chen, Y. (2013). Recent climate changes over the Tibetan Plateau and their impacts on energy and water cycle: A review. *Global and Planetary Change*, *112*(1), 79–91. <https://doi.org/10.1016/j.gloplacha.2013.12.001>
- Yang, S. H., Li, R., Wu, T. H., Wu, X. D., Zhao, L., Hu, G., et al. (2021). Evaluation of soil thermal conductivity schemes incorporated into CLM5.0 in permafrost regions on the Tibetan Plateau. *Geoderma*, *401*, 115330. <https://doi.org/10.1016/j.geoderma.2021.115330>
- Yang, Z. L., Dickinson, R. E., Henderson Sellers, A., & Pitman, A. J. (1995). Preliminary study of spin-up processes in land surface models with the first stage data of project for intercomparison of land surface parameterization schemes phase 1(a). *Journal of Geophysical Research*, *100*(D8), 16553–16578. <https://doi.org/10.1029/95JD01076>
- Yuan, Y., Ma, Y. M., Zuo, H. C., Yang, C. Y., Yuan, L., & Chen, J. L. (2021). Modification and comparison of thermal and hydrological parameterization schemes for different underlying surfaces on the Tibetan Plateau in the warm season. *Journal of Geophysical Research: Atmospheres*, *126*, e2021JD035177. <https://doi.org/10.1029/2021JD035177>
- Zhang, P., Zheng, D., van der Velde, R., Wen, J., Ma, Y., Zeng, Y., et al. (2022). A dataset of 10-year regional-scale soil moisture and soil temperature measurements at multiple depths on the Tibetan Plateau. *Earth System Science Data*, *14*(12), 5513–5542. <https://doi.org/10.5194/essd-14-5513-2022>
- Zhang, X. D., Huang, A. N., Dai, Y. J., Li, W. P., Gu, C. L., Yuan, H., et al. (2022). Influences of 3D sub-grid terrain radiative effect on the performance of CoLM over Heihe River Basin, Tibetan Plateau. *Journal of Advances in Modeling Earth Systems*, *14*, e2021MS002654. <https://doi.org/10.1029/2021MS002654>
- Zhong, L., Ma, Y. M., Salama, M. S., & Su, Z. B. (2010). Assessment of vegetation dynamics and their response to variations in precipitation and temperature in the Tibetan Plateau. *Climatic Change*, *103*(3–4), 519–535. <https://doi.org/10.1007/s10584-009-9787-8>
- Zou, D., Zhao, L., Sheng, Y., Chen, J., Hu, G., Wu, T., et al. (2017). A new map of permafrost distribution on the Tibetan Plateau. *The Cryosphere*, *11*(6), 2527–2542. <https://doi.org/10.5194/tc-11-2527-2017>